AFRL-AFOSR-UK-TR-2020-0013

Quantification of Combustion Regime Transitions to Distributed Modes

Rune Peter Lindstedt
IMPERIAL COLLEGE OF SCIENCE TECHNOLOGY & MEDICINE
EXHIBITION RD
LONDON, SW7 2BT
GB

05/19/2020
Final Report

Air Force Research Laboratory
Air Force Office of Scientific Research
European Office of Aerospace Research and Development
Unit 4515 Box 14, APO AE 09421

REPORT DOCUMENTATION PAGE

Form Approved
OMB No. 0704-0188

1. REPORT DATE *(DD-MM-YYYY)*	2. REPORT TYPE	3. DATES COVERED *(From - To)*
09-04-2020	Final Technical Report	15/01/2017 - 14/01/2020

4. TITLE AND SUBTITLE
Quantification of Combustion Regime Transitions to Distributed Modes

5a. CONTRACT NUMBER
FA9550-17-1-0021

5b. GRANT NUMBER

5c. PROGRAM ELEMENT NUMBER

6. AUTHOR(S)
Fabian Hampp and R. Peter Lindstedt

5d. PROJECT NUMBER

5e. TASK NUMBER

5f. WORK UNIT NUMBER

7. PERFORMING ORGANIZATION NAME(S) AND ADDRESS(ES)
Department of Mechanical Engineering, Imperial College, Exhibition Road, London SW7 2AZ, UK

8. PERFORMING ORGANIZATION REPORT NUMBER
Final Report FA9550-17-1-0021 (MEFL_P60281)

9. SPONSORING/MONITORING AGENCY NAME(S) AND ADDRESS(ES)
Dr Douglas Smith CIV USAF AFMC AFOSR/IOE, (314) 235-6013, email: douglas.smith.82@us.af.mil; (Dr Russell Cummings, AFOSR/IOE, (314) 235-6021). Address: 86 Blenheim Crescent, Ruislip, Middlesex HA47HB, UK; Dr Chiping Li, DR-04 USAF AFMC AFOSR/RTA, email: chiping.li@us.af.mil.

10. SPONSOR/MONITOR'S ACRONYM(S)

11. SPONSOR/MONITOR'S REPORT NUMBER(S)

12. DISTRIBUTION/AVAILABILITY STATEMENT
UU

13. SUPPLEMENTARY NOTES

14. ABSTRACT
Combustion in the absence of sharp flame fronts has significant advantages in terms reduced signatures and improved fuel efficiency resulting in increased range. The operating conditions often exceed conventional extinction criteria and typically require careful aerodynamic balancing for sustained chemical activity. The work shows that low Damköhler numbers lead to a separation of reaction zones, flame structures that are distinctly different from those associated with burning in the flamelet regime, that turbulent mixing of separated reaction zones can be expected to become of significant importance and that conventional combustion regime diagrams are inadequate.

15. SUBJECT TERMS
Turbulent Premixed Flames; Multi–Fluid Statistics; Fuel Effects; Combustion Chemistry; Damköhler Number Scaling; Auto-ignition Based Combustion; Flameless Combustion

16. SECURITY CLASSIFICATION OF:			17. LIMITATION OF ABSTRACT	18. NUMBER OF PAGES	19a. NAME OF RESPONSIBLE PERSON
a. REPORT	b. ABSTRACT	c. THIS PAGE			R. Peter Lindstedt
U	U	U	UU	58	19b. TELEPHONE NUMBER *(Include area code)* +44-207-594 7039

Final Report FA9550-17-1-0021

Quantification of Combustion Regime Transitions to Distributed Modes

Period of Performance: January 15, 2017 to Jan 14, 2020

F. Hampp and R. P. Lindstedt[*]
Department of Mechanical Engineering, Imperial College, Exhibition Road, London SW7 2AZ, UK

[*]Principal Investigator, email: p.lindstedt@imperial.ac.uk

Contents

List of Figures

List of Tables

Summary

In order to fulfil increasingly stringent regulations on emission of oxides of nitrogen and particulates, novel combustion devices increasingly operate in the absence of distinct flame fronts e.g. via flameless combustion modes. The approach has potentially significant advantages in terms reduced signatures and improved fuel efficiency resulting in increased range. The operating conditions often exceed conventional extinction criteria and require thermal support and/or careful aerodynamic balancing for sustained chemical activity.

The final report for Grant Award FA9550-17-1-0021 outlines work performed to quantify the transition to distributed combustion modes that no longer adhere to the conventional bimodal distribution of reactants and products characterised by a negligible probability of finding intermediate fluid states. This was achieved through the experimental quantification of the probability of encountering at least five separate fluid states (e.g. reactants, combustion products, mixing fluid, fluids with low and high chemical reactivity) as a function of the Damköhler (Da) number$^{(a)}$ through the use of simultaneous Mie scattering, OH-PLIF and PIV. The flames were aerodynamically stabilised flames in a back–to–burnt opposed jet configuration, featuring fractal grid generated multi-scale turbulence (Re $\simeq$ 18,400 and Re$_t$ $>$ 370), due to the exceptional control and flexibility of the configuration. The chemical timescale was varied via the mixture stoichiometry resulting in a wide range of Damköhler numbers ($0.08 \leq$ Da ≤ 5.1) with the nominal mode transition point at $Da \simeq 1$. The approach was further used to analyse the underlying conditions for burning mode transitions$^{(b)}$ and it was shown that self-sustained flames can exist low strain regions. By contrast, in highly strained regions (e.g. beyond the conventional extinction point) the burning mode is governed by enthalpy support resulting in increased levels of vorticity and an absence of a preferential dilatation direction.

Deviations from conventional bimodal flame structures for $Da < 1$ were further analysed$^{(c)}$ by quantifying the impact of the external enthalpy support by varying the temperature from $1200 \leq \ T_{HCP}$ (K) ≤ 1600. The diagnostics were extended to include CH_2O–PLIF and the transition to spatially distributed chemical reactions to reaction zones was further quantified. It was shown that flamelet-like structures are only present at high T_{HCP} following the onset of high temperature chain branching reactions. By contrast, the low temperature chemistry is continuously active with CH_2O increasingly more spatially distributed with reducing support temperature. The work extended the multi-fluid probability statistics by investigating the structure of formaldehyde and hydroxyl layers with their cross–correlation used to identify heat release layers. The impact of the fuel chemistry on burning mode transitions was also investigated$^{(d)}$ using premixed dimethyl ether (DME), ethanol (EtOH) and methane (CH_4) flames for equivalence ratios $0 \leq \Phi \leq 1$ resulting in a

Damköhler number range $0.06 \leq Da \leq 5.1$. The use of DME and ethanol follows the need to establish the level of impact of substantially different fuel oxidation pathways. The fuels are isomeric forms (CH_3-O-CH_3 and CH_3-CH_2-OH) with the same elemental composition (H_6C_2O) and effectively the same transport properties yet with profoundly different combustion characteristics (ie. Diesel (DME) and gasoline (EtOH) replacements). The external enthalpy support was kept constant (T_{HCP} = 1700 K) along with the level of turbulence. A more rapid transition towards self-sustained (e.g. flamelet type) combustion was observed for DME. By contrast, the transition was significantly delayed for methane with EtOH showing an intermediate behaviour. The strain rate distribution on the reactant fluid surface remained similar to the (non-reactive) mixing layer for stoichiometric methane flames, while the corresponding DME and EtOH flames detach from the stagnation plane leading to stablisation in lower compressive strain rate regions.

Overall, the work performed shows that low Damköhler numbers lead to a separation of reaction zones and flame structures that are distinctly different from those associated with burning in the flamelet regime of combustion. The work further suggests that turbulent mixing of separated reaction zones can be expected to become of significant importance and merit further investigation. It has also been shown that conventional combustion regime diagrams are inadequate, that auto-ignition based combustion may become a feature and that corresponding Damköhler number definitions are required. Autoignition based combustion regimes are dominant in augmentors, may become dominant in advanced gas turbines and are in need of further quantification.

Selected quoted references acknowledging support from Grant FA9550-17-1-0021.

(a) F. Hampp, R.P. Lindstedt, Strain distribution on material surfaces during combustion regime transitions, Proc. Combust. Inst. 36 (2017) 1911-1918.

(b) F. Hampp, R.P. Lindstedt, Quantification of combustion regime transitions in premixed turbulent DME flames, Combust. Flame 182 (2017) 248-268.*

(c) F. Hampp, S. Shariatmadar, R.P. Lindstedt, Quantification of low Damköhler number turbulent premixed flames, Proc. Combust. Inst. 37 (2019) 2373-2381.

(d) F. Hampp, R.P. Lindstedt, Quantification of fuel chemistry effects on burning modes in turbulent premixed flames, Submitted to Combust. Flame, Revised February 2020.

* Awarded the Sugden Prize for the most significant UK contribution to combustion research in 2017 by the Combustion Institute (British Section).

1 Introduction

State-of-the-art combustion technologies, e.g. spark ignition engines and gas turbines for power generation, operate under conditions where turbulence governs (partially-) premixed flame propagation [1]. Related burning modes can exhibit a flamelet-like structure characterised by fast chemical timescales (τ_c) [2] with Damköhler numbers (Da) generally above unity. Savard and Blanquart [3] estimate that the flamelet assumption is valid with reasonable accuracy for Karlovitz numbers (Ka) < 10. The modelling of premixed turbulent flame propagation under such conditions is one focal point of combustion research [1] with the underlying flamelet assumption providing the basis for developments such as the Bray-Moss-Libby (BML) [4], coherent flame [5] and level set [6] models. In order to fulfil increasingly stringent regulations on NOx and particulate emissions, novel combustion devices increasingly operate in the absence of distinct flame fronts e.g. via flameless combustion modes [7]. The approach has potentially significant advantages in terms reduced signatures and improved fuel efficiency resulting in increased range. The operating conditions often exceed conventional extinction criteria and require thermal support, e.g. from exhaust gases [8], for sustained chemical activity. Practical examples that realise stable fuel-lean operation at low Da include flameless oxidation gas turbine engines [9] and industrial furnaces [10]. Minamoto et al. [11] investigated the reaction zone structure under flamelet and moderate or intense low-oxygen dilution (MILD) conditions using direct numerical simulation (DNS). The data showed the coexistence of thin and fragmented flamelets with spatially distributed chemical reactions. The broadening or fragmentation of a reaction zone is strongly dependent on the chemical timescale. A mixture with low reactivity (e.g. low equivalence ratio or high dilution levels) requires substantially reduced turbulence levels [12] to alter the reaction zone away from a bimodal structure. The blending of hot diluents with extremely fuel rich or lean mixtures can lead to conditions where the chemical timescale dominates the interaction with the turbulent flow [13] and where the combustion chemistry assumes a decisive role [3, 11, 14]. Duwig et al. [15] investigated reaction zone broadening of vitiated methane/air jet flame with significant differences for lean (Φ = 0.4, 0.8) and rich (Φ = 6.0) conditions observed. A deep penetration of the CH and HCO radicals into the OH layer and a CH layer broadening of up to an order of magnitude compared to the laminar thickness was observed by Zhou et al. [12, 16, 17, 18]. Goh et al. [19] investigated the transition to flameless oxidation of fuel lean premixed JP-10 (exotetrahydrodicyclopentadiene) flames using a back-to-burnt (BTB) opposed jet configuration and compared to corresponding twin flames approaching extinction [20].

As part of Grant Award FA9550-17-1-0021 Hampp and Lindstedt [21] initially quantified the probability of encountering up to five separate fluid states (reactants, combustion

products, mixing fluid, fluids with low and high reactivity) in premixed turbulent DME flames as a function of the Damköhler number. The flames were aerodynamically stabilised in a back–to–burnt opposed jet configuration featuring fractal grid generated multi-scale turbulence (Re $\simeq$ 18,400 and $\mathrm{Re}_t > 370$). The chemical timescale was varied via the mixture stoichiometry resulting in a wide range of Damköhler numbers ($0.08 \leq \mathrm{Da} \leq 5.1$). The mean turbulent strain ($\geq 3750\ \mathrm{s}^{-1}$) exceeded the extinction strain rate of the corresponding laminar flames for all mixtures. Simultaneous Mie scattering, OH-PLIF and PIV were used to determine the probability of encountering the different fluid states. For mixtures where the bulk strain ($\simeq 750\ \mathrm{s}^{-1}$) was close to (or less than) the extinction strain rate, fluids with low and high reactivity were segregated by introducing thresholds based on the OH concentration at extinction. The sensitivity of the distribution between the fluid states to the thresholds was also evaluated. The flow conditions were further analysed in terms of Damköhler and Karlovitz numbers based on chemical time scales corresponding to laminar flames and auto–ignition events. It was shown that a multi–fluid approach can be used to quantify combustion regime transitions of relevance to low polluting combustion technologies. The study provided (i) the evolution of multi–fluid probability statistics as a function of the Damköhler number, (ii) mean flow field statistics, (iii) conditional velocity statistics and (iv) a tentative combustion regime classification.

Hampp and Lindstedt [22] subsequently analysed the underlying conditions for burning mode transitions from close to the corrugated flamelet regime to distributed reactions. Turbulent ($\mathrm{Re}_t \simeq 380$) premixed DME/air flames were aerodynamically stabilised in the same opposed jet configuration with the Damköhler number varied through the mixture stoichiometry. The analysis showed self-sustained flames in low strain regions with a collocated flow acceleration for higher Damköhler numbers. By contrast, in highly strained regions (e.g. beyond the twin flame extinction point) the burning mode was governed by the counter-flowing hot combustion products resulting in increased levels of vorticity and an absence of a preferential dilatation direction. The analysis provided novel insights into combustion regime transitions by means of (i) strain rate statistics conditioned upon material surfaces and (ii) the evolution of fluid state interface probabilities as a function of the Damköhler number. The work further showed (iii) that the combustion mode influences scalar transport and that increased levels of turbulence retards the transition to non-gradient transport. The above work [21, 22] found that high Da counterflow flames exhibit a clear flamelet-like structure with steep gradients and a distinct dilatation direction. By contrast, the low extinction strain rates typically associated with low Da flames prevented conventional flame propagation leading to a strong deviation from a bimodal structure and OH gradients well below the (theoretical) flamelet limit due to turbulent transport. The burning mode and reaction progress of such flames becomes dominated by

the thermochemical state of the external enthalpy support. The use of external enthalpy support (e.g. via heat recirculation) can enable stable combustion under highly strained conditions or at low Damköhler numbers and lead to significantly reduced emissions and fuel consumption. However, the flame structures deviate from the conventional bimodal flame structure and chemically active fluid states become statistically relevant. Hampp and Lindstedt [23] quantified the impact of such support on the combustion of lean (Φ = 0.6) turbulent premixed DME / air flames with a Damköhler number around unity. The bulk strain (a_b = 750 s^{-1}) slightly exceeded the extinction strain rate (a_q = 600 s^{-1}) of the corresponding laminar opposed twin flame with the mean turbulent strain (a_I = 3200 s^{-1}) significantly higher. The HCP temperature ($1600 \leq T$(K) ≤ 1800) was varied from close to the extinction point ($T_q \simeq$ 1570 K) of the corresponding laminar twin flame to beyond the unstrained adiabatic flame temperature ($T_{ad} \simeq$ 1750 K). The flames were characterised using simultaneous Mie scattering, OH-PLIF and PIV measurements and subjected to a multi-fluid analysis (i.e. reactants and combustion products, as well as mixing, weakly reacting and strongly reacting fluids). The study quantified the (i) evolution of fluid state probabilities and (ii) interface statistics, (iii) unconditional and (iv) conditional velocity statistics, (v) conditional strain along fluid interfaces and (vi) scalar fluxes as a function of the external enthalpy support. The work showed, among other matters, that the presence of strongly reacting fluid elements nearly vanished as the support temperature approached that of the extinction temperature of the corresponding twin flame. Hampp and Lindstedt [24] extended the multi-fluid analysis in order to quantify the impact of such conditions on a turbulent ($Re_t \simeq 350$) lean (Φ = 0.50) premixed DME / air flame with $Da \simeq 0.29$. The flames were aerodynamically stabilised in the back-to-burnt opposed jet configuration with the temperature of the external enthalpy support varied from $1200 \leq T_{HCP}$ (K) ≤ 1600. Simultaneous Mie scattering, CH_2O and OH – PLIF and PIV were used to quantify the transition from spatially distributed chemical reactions to reaction zones that appear flamelet-like. The analysis showed that in the current configuration such structures are only present at high T_{HCP}. By contrast, the low temperature chemistry is continuously active with CH_2O increasingly more spatially distributed with reducing support temperature. The analysis provided novel insights into low Damköhler number combustion and burning mode transitions by means of (i) multi-fluid probability statistics, (ii) the structure of formaldehyde and hydroxyl layers and (iii) their cross–correlation as well as (iv) the underlying strain rate statistics on material surfaces. It can be noted that while the flames exhibited very different characteristics depending on the level of enthalpy support, the nominal Da number was unchanged thus highlighting the need for additional definitions.

External enthalpy stabilised combustion exhibits complex turbulence–chemistry interactions that may lead to a competition between auto-ignition related oxidation and con-

ventional flame propagation [25]. While laminar burning properties of many hydrocarbon fuels are similar, the auto-ignition delay time can vary by multiple orders of magnitude. Sabia et al. [26, 27] investigated propane auto-ignition for a wide range of MILD conditions and noted a strong inert gas dilution effect. Fuel lean prevaporised acetone, ethanol and n-heptane were investigated by Ye et al. [28] in a MILD combustor with distinct differences in flame stability observed. Chen et al. [29] studied the high temperature ignition of dimethyl ether (DME)/methane (CH_4)/air blends. Small amounts of DME addition resulted in advantageous combustion characteristics due to significantly reduced ignition delay times and augmented strain resilience. Wang et al. [30, 31] explored the extinction characteristics of premixed and non-premixed DME and ethanol (EtOH) flames in an opposed jet geometry with DME showing a higher strain resilience than EtOH.

In addition to presenting selected results from a variation in the external enthalpy, the present report is focused on a quantification of the impact of combustion chemistry on burning mode transitions through the use of of DME, EtOH and CH_4 over a wide range of Damköhler ($0.06 \leq Da \leq 5.1$) numbers [32]. Combustion regime transitions were obtained by means of chemical timescale adjustments with $0.2 \leq \Phi \leq 1.0$ under constant turbulence conditions ($Re_t \simeq 361 \pm 12$) and external enthalpy support ($T_{HCP} = 1700$ K). The choice of DME (Diesel replacement) and EtOH (spark ignition engine replacement) was based on their relevance as alternative automotive fuels [33, 34], similar laminar flame properties and significantly different auto-ignition characteristics [35] with their relatively well established chemistries [36] an advantage. It should be emphasised that the use of DME and EtOH was due to the very different combustion characteristics and the need to establish the level of impact of the different oxidation pathways in an unambiguous manner. The fuels are isomeric forms (CH_3-O-CH_3 and CH_3-CH_2-OH) with the same elemental composition (H_6C_2O) and effectively the same transport properties yet with profoundly different combustion characteristics. These fuels can be replaced by increasingly complex hydrocarbons leading up to aviation fuels, such as JP-10 [19], that highlight additional complexities. Methane is extensively used in gas turbines for power generation and was selected to provide reference cases. The impact of the fuel reactivity on the burning mode transition was investigated via a multi-fluid description [21]. Information on the conditions leading to burning mode transitions via (i) multi-fluid probabilities, (ii) turbulence-flame interactions delineated by means of conditional velocity statistics and (iii) strain along fluid iso-contours. The fuel chemistry differences are shown to cause large changes in conditional velocity statistics and the impact is hence not subtle. Consequently, in addition to such findings, the data are expected to be particularly valuable for the development of models applicable to combustion processes that transition to distributed modes.

1.1 Specific Objectives

Project FA9550-17-1-0021 features extended studies that permit a delineation of combustion regimes and the impact on the associated chemical pathways leading to fuel conversion. The work covered extended studies that have permitted a general delineation of combustion regimes in the context of relevant flow-field physics. A principal objective was to provide a route leading to a quantitative evaluation of the relative importance of flow and high temperature chemistry regions in the context of combustion regime transitions under reduced peak temperature conditions. The principal objectives of the research programme can be summarised as:

- Analyse the relative importance of low temperature chemistry by extending the quantification of the transition to a distributed combustion mode using simultaneous OH/CH_2O/Rayleigh thermometry measurements and simultaneous OH/CH_2O/PIV (e.g. Hampp et al. [24]).
- Extend the parameter range investigated to include substantial changes in conditions that lead to an increased influence of auto-ignition supported combustion modes and a corresponding reduction in the associated Damköhler numbers (e.g. Hampp et al. [21, 23].
- Determine the probability distribution of temperature and rate of strain on flame surfaces in regions with evidence (e.g. via elevated CH_2O concentrations) of low temperature chemistry (e.g. Hampp and Lindstedt [22] and Hampp et al. [24]).
- Identify the dominant chemical pathways and combustion characteristics, using detailed chemistry, under the conditions determined experimentally as relevant (e.g. Hampp and Lindstedt [21]).
- Extend the current fuel matrix to include a fuel that features distinct low temperature chemistry and contrast with fuels that do not [32].

The work performed directly relates to the BAA-AFRL-AFOSR-2015-0001 call for work on key turbulent combustion phenomena and game-changing energy conversion processes (combustion at extreme time-scales). The fuels used, methane, dimethyl ether (a potential Diesel fuel replacement) and ethanol (a spark ignition engine fuel replacement) span a significant reactivity range [32]. Ethanol and DME have very different combustion characteristics and were used to establish the level of impact of the different oxidation pathways for fuels of practical relevance. Methane is extensively used in gas turbines for power generation and serves as a foundation for the extension of past studies of aviation fuels such as JP-10 [19].

2 Methods, Assumptions and Procedures

The current BTB opposed jet configuration has distinct advantages for the systematic investigation of burning mode transitions from flamelet-like structures towards distributed reaction zones. These include (i) relatively well developed turbulence [38, 39]; (ii) separate control of chemical and turbulent timescales [40]; (iii) adjustable boundary conditions [41]; (iv) excellent optical access [38, 42]; (v) flame stabilisation related to the intrinsic aerothermochemistry [21, 22, 43]; and (vi) a well controlled burnt gas state to stabilise flames beyond conventional extinction condition [21].

2.1 Measurement Setup

The cross fractal grid (CFG) opposed jet configuration, schematically depicted in Fig. 1, was operated in a back-to-burnt mode. The original facility was developed by Geyer et al. [42]. Geipel et al. [38] and Goh et al. [19, 20, 41] optimised the nozzle inflow geometry to eliminate low frequency instabilities [38, 44]. The use of CFGs [38] induced a turbulent flow field with multi-scale character [43] and realised a high turbulence to bulk strain ratio in absence of bulk flow instabilities [41]. The current optimal burner is identical to that used by Hampp et al. [21, 22, 45]. The nozzle separation (H) was set to one nozzle diameter (D = 30 mm).

Two separate gas mixing systems provided the reactants, i.e. dried and filtered Howden air, DME (99.9%), CH_4 (99.9%), H_2 (99%) and CO_2 (99%). Digital Bronkhorst mass flow controllers were used to control the reactant flow rates with an uncertainty $< 0.8\%$ at full scale [38]. Liquid ethanol (purity 99.9%) was injected by a feedback controlled rotary pump (Model LP132) and regulated by a Bronkhorst Cori-Flow M53 flow meter. The liquid fuel was mixed with a secondary air stream and evaporated using a temperature controlled Bronkhorst CEM W-303A unit [45]. The flow control system was operated via a purpose written LabView interface. Calibrated rotameters were used to regulate co-flow velocities to 30% of the upper nozzle (UN) bulk velocity [38].

The diagnostic setup, summarised below, has been discussed by Hampp and Lindstedt [21] including comprehensive uncertainty and error analyses. Simultaneous Mie scattering, PIV and OH-PLIF measurements were conducted using the barium nitrate crystal technique of Kerl et al. [46]. The two superimposed light sheets (532 nm and 281.7 nm) exhibited a height of 1D and thickness < 0.25 mm and < 0.50 mm, respectively. The Mie scattering signal was recorded using a LaVision ProX 4M camera (2×2 binning) equipped with a Tokina AF 100 mm lens (f/2.8) and narrow bandpass filter (3 nm centred at 532 nm). A dichroic beam splitter was used to spectrally separate the OH fluorescence signal from the Mie scattering. The OH signal was recorded using an interline-transfer

CCD-camera (LaVision Imager Intense) connected to an intensified relay optics (LaVision IRO) unit. The IRO was equipped with a 105 mm ultraviolet lens (f/2.8) from LaVision. The used filter combination created a bandpass with a transmissivity $> 85\%$ from 300 – 320 nm and an optical density > 5 to block the laser lines. A temporal separation of 25 μs between the PIV laser pulses was found ideal to minimise spurious vectors. The OH-PLIF images were obtained from the first pulse. Aluminium oxide powder ($d_{p,50}$ = 0.44 μm and $d_{p,90}$ = 1.7 μm) was used as a velocity tracer with both nozzles seeded separately.

In addition, Hampp et al. [24] performed simultaneous Mie scattering, PIV, CH_2O and OH – PLIF measurements using the 2^{nd} harmonic of a Litron Nano LG 175-10 Nd:YAG (Mie scattering and PIV) and a frequency tripled Spectra Physics Quanta-Ray Lab-150 Nd:YAG (CH_2O – PLIF) laser. The residual 2^{nd} harmonic of the latter light source was used to pump a Sirah Cobra Stretch dye laser to probe OH via the $Q_1(8)$ line. The three spatially overlapped light sheets (i.e. Mie scattering and PIV at 532 nm, light sheet height H_{LS} = 27 mm, pulse power $P_l \simeq$ 30 mJ; CH_2O – PLIF at 355 nm, H_{LS} = 18 mm, $P_l \simeq$ 150 mJ; OH – PLIF at 283.55 nm, H_{LS} = 18 mm, $P_l \simeq$ 14 mJ) were located symmetrically around the theoretical stagnation plane. The light sheet thickness was estimated to $\sim$100 µm in the centre of the interrogation region using burn marks. The first pulse of the Mie scattering was recorded 200 ns prior to the LIF signals in order to eliminate elastic scattering in the LIF detection systems. Dichroic filters were used to spatially and spectrally segregate the signals. The PIV camera (LaVision LX 8M) was equipped with a 180 mm f/2.8 Sigma lens and a narrow width bandpass filter centred at 532 nm. Two LaVision intensifier relay optic units and imager intense cameras were used to the record the CH_2O and OH – PLIF signals. The former was equipped with a 85 mm (f/1.2) lens and a 400 nm long-pass filter due to the absence of polycyclic aromatic hydrocarbons (PAH) interference [47]. The OH – PLIF was recorded using a 105 mm UV lens (f/2.8) and a filter combination that featured an optical density above 5 for all laser lines and a transmissivity in excess of 85% from 300–320 nm. An intensifier gate time of 50 ns and a low gain level of 60% minimised flame luminescence and noise. The detection system was calibrated using a multi-frequency target.

Cross-correlation PIV with decreasing interrogation regions size (128 $\times$ 128 to 48 $\times$ 48 with a 75% overlap) was conducted using LaVision Davis 8.1. A high accuracy mode with adaptive interrogation window shape modulation was used for the final pass [48]. The velocity field was resolved by 115 $\times$ 88 vectors, providing a spacing of 0.30 mm and spatial resolution of 0.60 mm [21]. A minimum of 3000 realisations per condition were recorded to achieve statistical independence. Pre-processing steps of the recorded images (i.e. alignment, data reduction, noise reduction, shot-to-shot intensity fluctuations and white image correction) were described by Hampp et al. [21, 45]. Predefined interro-

gation windows close to the upper and lower nozzle exit were used to obtain well defined calibration data [21].

2.2 Flow Conditions

The premixed fuel / air mixtures [32] were injected through the upper nozzle and stabilised against hot combustion products (HCP) emerging the lower nozzle. The flow conditions are summarised in Table 1 and detailed below.

2.2.1 Upper Nozzle Conditions

The CFG was installed 50 mm upstream of the UN exit providing a relatively well developed turbulent flow field [38]. The grid features a blockage ratio of 65% with a maximum to minimum bar width ratio of t_r = 4. The equivalence ratio of the premixed fuel / air mixtures was varied from $0.20 \leq \Phi \leq 1.0$ with the mixing layer ($\Phi = 0$) case also investigated. The volumetric reactant mixture flow rate was maintained constant at $\dot{V}_{UN} \simeq 7.07 \times 10^{-3}$ m^3 s^{-1} (at STP). In order to avoid re-condensation of ethanol, the reactants were preheated to T_r = 320 K [45]. This resulted in a constant bulk velocity at the nozzle exit of U_b = 11.2 m s^{-1}, a bulk strain rate of $a_b = 2 \cdot U_b / H \simeq 750$ s^{-1} and a turbulent strain ≥ 3200 s^{-1} [21]. The current flow conditions realised a constant $Re \simeq$ 19,550 with $Re_t \simeq 361 \pm 12$. The turbulent Reynolds number was determined based on an integral length scale of turbulence (L_I = 3.9 $\pm$ 0.2 mm) and velocity fluctuations ($u_{rms} \simeq$ 1.6 m s^{-1}) measured at the UN exit using hot wire anemometry [24]. The latter value is within 10% of the velocity fluctuations measured via PIV 1 mm away from the UN nozzle exit and assuming locally axisymmetric turbulence, i.e. $u_{rms} = 1/3(u' + 2 \cdot v')$, where u' and v' are the axial and radial velocity fluctuations, respectively. The variation of the burnt gas state temperature was conducted for a premixed DME / air at Φ = 0.50 with a $Re_t \simeq 350$, $Da \simeq 0.29$ and Ka = 64.

2.2.2 Lower Nozzle Conditions

The lower nozzle burnt gas state was obtained using premixed stoichiometric H_2/air flames diluted with 22% CO_2 by volume prior combustion to control the temperature. The flames were stabilised on a mesh (FSM: blockage ratio 62%, aperture 0.40 mm, wire thickness 0.25 mm) [22]. A second finer mesh acted as flashback arrestor (FBA). The mesh combination was installed 100 mm upstream of the nozzle exit. The nozzle exit temperature was set to T_{HCP} = 1700 $\pm$ 3.5 K, measured via a 50 μm type R thermocouple, with an estimated heat loss of 10% to the burner assembly [21]. The stagnation plane was located

in the proximity of the burner centre by matching jet nozzle momenta via a burnt gas velocity of 24 m s^{-1}. The long residence time ($\sim$6 ms) of the burnt gases in the lower nozzle provides hot combustion products in close-to thermochemical equilibrium at the exit and the products consist primarily ($>$ 99.8 %) of N_2, O_2, H_2O and CO_2. Consequently, the OH concentration of the HCP is constant with a computed value of $[OH]^{\ddagger} \approx 8.82 \times$ mol m^{-3} and a clearly detectable OH fluorescence intensity ($I^{\ddagger}$) with a signal to noise ratio (SNR) = 3.5 [21]. The measured $I^{\ddagger}$ and computed $[OH]^{\ddagger}$ provide well defined reference values used to calibrate the applied OH intensity segregation technique [21].

In addition, deviations from conventional bimodal flame structures for $Da < 1$ were further analysed by Hampp et al. [24]. In this context, the impact of the external enthalpy support was quantified by varying the temperature from $1200 \leq \ T_{HCP}$ (K) ≤ 1600 via the equivalence ratio (Φ) and H_2 / CH_4 blending ratio (see Table 2). The addition of CH_4 to H_2 / air flames broadens the regime of stable flame anchoring on the perforated plate (PP) by eliminating instabilities of the lower nozzle flame. The PP had a 50% blockage ratio with 1.0 mm diameter holes and was located 100 mm upstream of the lower nozzle exit. Flames could not be stabilised on the perforated plate below 1200 K and this defined the lower T_{HCP} limit. The upper limit of 1600 K was above the weakly strained (75 s^{-1}) adiabatic flame temperature (T_{ad} = 1536 K) of the upper nozzle reactants. Differences in the HCP density were compensated by jet momentum matching and modest adjustments of the HCP bulk velocity (see Table 2).

2.3 Data Analysis Procedures

2.3.1 Chemical Timescales and Limiting Conditions

The current experimental conditions provide both thermally supported and self-sustained flames [21, 22]. The latter, higher Da flames, detach from the stagnation plane and anchor in low strain regions. With reducing Da, the strain acting on the flame surface increasingly results in local extinction, with global extinction prevented by the turbulent transport of HCP fluid across the stagnation plane [19, 22, 49]. Chemical timescales and laminar flame properties were determined computationally to support the analysis of experimental data in terms of non-dimensional groups (e.g. Da numbers). The reaction mechanism of Park [36] was used in combination with the hydrogen chemistry of Burke et al. [50]. The mechanism was validated against laminar burning velocities [51, 52, 53] and species profiles [54, 55] by Park [36] and auto-ignition delay times (τ_{ign}) by Hampp [45] with good agreement. The calculations were further validated here for flame extinction using experimental data from Wang [31] for DME and EtOH and Law et al. [56] for CH_4 with good agreement as shown in Table 3.

Strained Laminar Flame Extinction Points

Self-sustained high Da flames decouple from the external enthalpy support and conventional aerothermochemistry criteria apply. A minimum (critical) integrated heat release rate ($\int \dot{Q}_q$) was found to be required for self-sustained flame propagation [21]. Values of $\int \dot{Q}_{BTB} < \int \dot{Q}_q$ led to flame extinction in the twin flame or thermally supported burning in the back-to-burnt configuration. The thermochemical state (e.g. peak temperature and peak species concentrations of OH, CH and CH_2O) of self-sustained burning flames was well correlated with $\int \dot{Q}$ and segregated self-sustained from thermally supported burning in BTB flames. Strained laminar counterflow calculations [57] provided the chemical timescales and flame properties as a function of equivalence ratio and fuel type. The computational domain was well resolved with > 25 cells across the CH peak. The extinction strain (a_q) and peak OH concentration at extinction $[OH]_q$ were determined in a twin flame configuration with results in Table 4 along with the peak temperature at extinction (T_q) and $\int \dot{Q}_q$. The laminar burning velocity S_L and laminar flame thickness δ_f were determined using a BTB configuration (corresponding to the experiment) with results in Table 5. The extinction strain of low Da flames (i.e. Φ = 0.2) was significantly lower than the strain conditioned on the reaction onset iso-contour [22] and data thus excluded.

Flame Parameters and Dimensionless Groups

The Re_t was maintained constant in the current study. The Damköhler and Karlovitz numbers, see Eq. (1), were varied by means of the chemical timescale (τ_c) through the equivalence ratio and fuel type.

$$Da = \frac{\tau_I}{\tau_c}\ ; \qquad Ka = \frac{\tau_c}{\tau_\eta} \tag{1}$$

The chemical timescale was obtained from the calculated laminar flame thickness (δ_f) based on the 5 – 95% fuel consumption layer [58] and the laminar burning velocity (S_L) as defined in Eq. (2). The integral timescale of turbulence (τ_I) was based on the measured u_{rms} = 1.6 m s^{-1} and L_I = 3.9 mm. The Kolmogorov timescale (τ_η) was estimated based on the rate of dissipation ($\varepsilon_r = u_{rms}^3 \cdot L_I^{-1}$) and the kinematic viscosity (ν_r) in the reactants with values listed in Table 5.

$$\tau_I = \frac{L_I}{u_{rms}}; \qquad \tau_c = \frac{\delta_f}{S_L}\ ; \qquad \tau_\eta = \sqrt{\frac{\nu_r}{\varepsilon_r}} \tag{2}$$

The resulting ranges of Damköhler numbers and Karlovitz numbers were $0.06 < Da < 5.1$ and $3.7 < Ka < 300$, respectively. The data can be readily plotted in a conventional Borghi diagram, see Fig. 2, to estimate the expected burning mode. The condi-

tions cover the range $3.2 \leq u_{rms}/S_L \leq 40$ with the intense turbulence regime limit $u_{rms}/S_L \simeq 19$ [59]. The ratio of the adiabatic to the initial reactant temperature (T_{ad}/T_r) decreases from 7.2 to 2.7 as the Da is reduced (see Table 5). The fuel reactivity is directly related to, and fully consistent with, the corresponding cetane number for DME or RON / MON numbers of EtOH and CH_4 as well as the spontaneous auto-ignition temperatures. DME is a diesel-like fuel with a high cetane number of 55 – 60 [60], while EtOH and methane exhibit high octane numbers, i.e. RON / MON of 110 / 90 [61] and > 120 [62], respectively. Hydrocarbon based aviation fuels can typically be expected to have combustion characteristics between these extremes. Spontaneous auto-ignition temperatures vary significantly at 508 [63], 642 [64], 868 K [65] for DME, EtOH and CH_4, respectively.

2.3.2 Multi–Fluid Post–Processing

Turbulence – chemistry interactions in low Da flows cannot be comprehensively quantified by bimodal (i.e. reactants and products) descriptions as combustion intermediates become statistically relevant [11]. Therefore we recently adopted a multi-fluid description that incorporates a wider range (e.g. mixing, weakly and strongly reacting fluids) of states [21, 22]. The methodology, briefly outlined below, was found instrumental for low Da flows and is here used to quantify fuel chemistry effects on burning mode transitions.

The current multi-fluid analysis used a conventional PIV tracer particle based density segregation technique, e.g. [43, 66, 67] in combination with a threshold based OH intensity band classification. The first threshold was based on experimental observations (see Λ_p below) and the second on well established combustion theories (see Λ_q in Sec. 2.3.2). For the conditions of interest, a linear relation was found sufficient (uncertainty $< 10\%$) to link relative theoretical OH concentrations to the experimentally observed fluorescence intensity and to identify characteristic intensity bands [21, 45, 68]. The fluids states are:

Reactants: Fresh reactants emerging from the UN that had not undergone any thermal alteration (i.e. no oxidation or mixing processes). The reactants were detected via a conventional PIV tracer particle based density segregation technique e.g. [43, 66, 67] capable of detecting multiple and fragmented splines.

Mixing fluid: A fluid state that had been exposed to a thermal change prior the onset of OH producing chemical reactions (i.e. via mixing with HCP). The mixing fluid was detected by the superposition of the Mie scattering and OH-PLIF image and was identified in regions with low seeding density and no OH signal.

Strongly reacting fluid: Regions with a high OH signal intensity consistent with self-sustained (e.g. flamelet) burning (see Sec. 2.3.2). Conventional extinction criteria apply [49, 69].

Weakly reacting fluid: A fluid state with modest levels of OH, e.g. ultra lean flames sustained by thermal support from an external enthalpy source and/or combustion products approaching equilibrium (see Sec. 2.3.2).

Hot combustion products: The HCP emerge from the lower nozzle in close–to chemical equilibrium at 1700 K and provide a well defined reference state with a constant OH concentration (see Sec. 2.3.1) and signal intensity ($I^{\ddagger}$) that was used to calibrate the OH band segregation. The maximum measured OH signal for a mixing layer case (Φ = 0.0) was used to separate the HCP from fluid elements containing OH originating from combustion with $\Phi > 0$. The limiting threshold $\Lambda_p = \lceil I/I^{\ddagger} \rceil$ = 2.0 was independent of the UN conditions (i.e. Φ and fuel type). The excess (1.0 $< I/I^{\ddagger} <$ 2.0) is from the oxidation of residual reactants contained in the HCP.

The density segregation technique, the delineation of the mixing fluid and the definition of the product fluid threshold (Λ_p) are identical to Hampp and Lindstedt [21]. The segregation of the weakly and strongly reacting fluids was extended, as outlined below, to accommodate the different fuels.

OH Containing Fluid States

The thermochemical state at the twin flame extinction point (e.g. $[\mathrm{OH}]_q$ see Table 4) segregates self-sustained from thermally supported burning in the current BTB configuration [21]. Regions with an OH fluorescence intensity ratio beyond the non-dimensional (extinction) threshold (see Table 4) defined by Eq. (3) were consequently assigned to the strongly reacting fluid (i.e. self-sustained burning).

$$\Lambda_{q(\Phi)} = \frac{[\mathrm{OH}]_{q(\Phi)}}{[\mathrm{OH}]^{\ddagger}} = \frac{I_{q(\Phi)}}{I^{\ddagger}} \qquad \forall \text{ fuels and } \Phi \geq 0.6 \tag{3}$$

The weakly reacting fluid (e.g. thermally supported burning) follows as $\Lambda_p < I/I^{\ddagger} < \Lambda_q$ and can originate from (i) ignition events, (ii) decaying OH concentration in combustion products or (iii) chemically active material that was diluted by the HCP.

Extended Multi-Fluid Analysis

Hampp et al. [22] considered the following three fluid states in addition to reactants and to combustion products due to the change in diagnostic setup:

Low Temperature Reactive (LTR) Fluid: Regions with a distinct CH_2O – PLIF signal in the absence of detectable OH levels [70].

Heat Release (HR) Fluid: The cross-correlation of CH_2O and OH – PLIF signals used to mark regions of heat release [71].

High Temperature Reactive (HTR) Fluid: Regions with an OH – PLIF signal ≥ 2 times the HCP OH intensity were used to delineate high temperature oxidation [21]. The HTR fluid thus combines the weakly and strongly reacting fluids defined above.

The above diagnostic and data processing methodology is applicable for all hydrocarbon based fuels and has recently been extended to include fuel rich ethylene flames with Poly-Aromatic Hydrocarbon (PAH) layers [72]. The latter is important in the context of aviation fuels with aromatic content and ethylene is also the dominant breakdown product of endothermic fuels as well as of conventional aviation fuels [73].

Multi-Fluid Fields and Velocity Conditioning

The superposition of the segregated fluid states (e.g. Mie scattering image into reactants and thermally altered fluid material and the three intensity bands of the OH – PLIF image into products, weakly and strongly reacting) yielded a multi-fluid image as exemplified in Fig. 3. The spatial resolution of the multi-fluid analysis was determined to $\lambda_{MF} \simeq 250$ μm, i.e. L_I / $\lambda_{MF} \simeq 16$ [21]. The mean scalar dissipation layer thickness ($\lambda_D = 11.2 \cdot L_I Re_t^{-3/4} Sc^{-1/2}$) [74] was resolved ($\lambda_D$ / $\lambda_{MF} \simeq 2.5$), while the Batchelor scale ($\lambda_B = L_\eta Sc^{-1/2}$) [75] was under-resolved (λ_B / $\lambda_{MF} \simeq 0.22$). Values for the Schmidt number (Sc) are listed in Table 5. Multi-fluid velocity conditioning (see Eq. (4)) was used to extend the analysis based on bimodal statistics [41, 43, 66, 67, 76].

$$
\begin{aligned}
\overline{U}_{k,FS,i,j} &= \frac{1}{N} \sum_{n=1}^{N} c_{FS,n,i,j} \cdot U_{k,n,i,j} \quad \forall\, i,j \\
(u'u')_{k,FS,i,j} &= \frac{1}{N} \sum_{n=1}^{N} c_{FS,n,i,j} \cdot \left(U_{k,n,i,j} - \overline{U}_{k,FS,i,j}\right)^2 \quad \forall\, i,j \\
C_{FS,i,j} &= \frac{1}{N} \sum_{n=1}^{N} c_{FS,n,i,j} \quad \forall\, i,j \\
\textstyle\sum_{FS} C_{FS} &\coloneqq 1
\end{aligned}
\tag{4}
$$

In Eq. (4), $c_{FS,n}$ is the instantaneous conditioning variable, i.e. unity within the fluid state (FS) and nil outside, k the velocity component, n the instantaneous image, N the number of images (3000) with i and j indices.

3 Results and Discussion

The multi-fluid probability and conditional velocity statistics were aligned at the first thermal alteration iso-contour (i.e. x_s = 0 and detected via the density segregation technique,

see Fig. 3) to eliminate modest variations of the stagnation plane location. The multi-fluid probabilities (Sec. 3.2) and conditional velocity statistics (Sec. 3.3) were evaluated along the theoretical stagnation point streamline (SPS), i.e. y = 0 in Fig. 3. The strain analysis in Sec. 3.5 was condition on y = 0 $\pm$ 1/2 L_I to include the radial movement of the stagnation point [38].

3.1 Detached and Self-Sustaining Flames

The leading edge of the $\overline{c}$ scalar field was determined from the statistics of the location of the $\overline{c} = 0.02$ iso-contour. Thus, for self-sustained flames $\overline{u^*} = \overline{u}|_{\overline{c}=0.02}$ [77] defined the corresponding turbulent burning velocity. However, for thermally supported low Da flames $\overline{u^*}$ corresponded to the velocity at the leading edge of the mixing layer. The $\Phi = 0.0$ case provided the reference for pure mixing in the absence of heat release and was located at $\overline{u^*}/u' = 2.7$. For the current conditions, the HCP influence became reduced for DME flames with $\Phi \geq 0.60$ and for stoichiometric EtOH flames as shown in row of values of $\overline{u^*}/u'$ listed in Table 5. By contrast, for methane the HCP influence remained dominant for all Φ. The above definition [77] can also be used to determine unique (not influenced by HCP support) turbulent burning velocities in the twin flame opposed geometry.

The gradual detachment of the flame from the stagnation plane was illustrated by the thickness of the layer δ_l defined as the distance between the axial position of the leading edge of $\overline{c}$ and the leading edge of the stagnation plane. The latter was determined from the statistics of the location of the HCP iso-contour. The mixing layer for the Φ = 0.0 case had a thickness δ_l/L_I = 0.23. With increasing Φ (i.e. Da) the leading edge of $\overline{c}$ shifted away from the stagnation plane. For DME, δ_l/L_I increased from 0.42 to 1.0 for Φ = 0.20 to 1.0, respectively. By contrast, the EtOH (CH_4) cases showed an attenuated detachment of δ_l/L_I = 0.17 (0.23) and 0.93 (0.52) for Φ = 0.20 and 1.0, respectively (see Table 5).

3.2 Multi-Fluid Probability Statistics

The reactant fluid probability, conditioned on the SPS and aligned at x_s = 0, was found to be fuel and equivalence ratio independent and has hence been omitted as the case of DME has been discussed by Hampp and Lindstedt [21].

3.2.1 Fuel Chemistry Effect on Multi-Fluid Probabilities

The mixing fluid probability ($P(m)$) exhibited distinct fuel type and Φ related differences as shown in Fig. 4, where the UN is at $x_s < 0$ and vice versa. The peak probability for low Da flames (i.e. $\Phi \leq 0.60$) was broadly constant for a given fuel with peak probabilities

of 0.9 for DME, 0.7 for CH_4 and 0.5 for EtOH. This reduction was repeatable and consistent [45]. The residual percentiles at $x_s = 0$ were allocated to the HCP fluid due to the low OH signal intensity consistent with this fluid state. Mixing layers with a thickness below the multi-fluid resolution were not considered. The DME mixing fluid peak probability and its spatial extent reduced significantly with increasing Da (i.e. Φ = 1.0) as chemical active fluid states were favoured. The EtOH mixing fluid showed the same trend, but with an attenuated reduction in $P(m)$ with increasing Da. By contrast, the need for thermal support for the CH_4 flames remained with a peak mixing fluid probability $\sim$70% for the stoichiometric case. The observation is consistent with the iso–contour based analysis relating to self–sustained flames presented in Sec. 3.1.

The weakly reacting fluid probability (P(w)) is also shown in Fig. 4 for all fuels. The DME and EtOH cases showed similar distributions with peak values increasing from $\sim$10 to 38% with Φ from 0.2 to 0.6. The shape and spatial variation of P(w) for CH_4 differed substantially from the oxygenated fuels, yet the increase in peak value was approximately maintained (5 – 27%). The probability tail showed a nearly linear decay for CH_4 compared to an exponential decay for DME and EtOH. The phenomena was repeatable [37] and was qualitatively also observed by Shen and Sutton [78]. For $Da > 1.0$, the peak of $P(w)$ reduced in favour of a gradual transition to the strongly reacting fluid – particular evident for DME. The weakly reacting fluid probability was only modestly reduced for EtOH and CH_4, which indicated the distinct need of thermal support to initiate and sustain chemical activity under current turbulence conditions.

The strongly reacting fluid probabilities $P(s)$ are also depicted in Fig. 4. At $Da \ll 1$ (i.e. Φ = 0.20) self–sustained combustion was not observed. With Da of $\mathcal{O}(1)$ at Φ = 0.60 peak probabilities of $P(s) \leq 20\%$ were obtained. The stoichiometric flames showed a substantial increase in the strongly reacting fluid for DME and EtOH and a modest increase for CH_4, realising peak probabilities of 72, 47 and 25%, respectively. The trend is consistent with the determined laminar flame extinction points listed in Table 4.

3.2.2 Burnt Gas Effect on Multi-Fluid Probabilities

The low temperature reactive (LTR) fluid is depicted in the top of Fig. 5. The peak probability of the presence of formaldehyde directly adjacent to the reactants was 92% for T_{HCP} = 1600 K and reduced gradually to 48% for T_{HCP} = 1200 K. The probability was gradually reduced away from the origin with increasing T_{HCP} as more reactive fluid states were favoured. The spatial extent of the low temperature reactive fluid at high T_{HCP} was effectively limited by the integral length scale of turbulence (L_I) as formaldehyde was consumed by high temperature reactions (e.g. $CH_2O \times OH$). By contrast, the tail of the LTR probability extended to $2{\cdot}L_I$ for low T_{HCP}. This was attributed to turbulent

transport away from the reaction onset as the thermochemical state favoured a persistent CH_2O concentration. The probability of the heat release fluid (i.e. $CH_2O \times OH$ cross-correlation) is depicted in the middle of Fig. 5. Peak probabilities of 11 and 34% were determined for T_{HCP} = 1500 and 1600 K, respectively, with a peak value around 5% for lower T_{HCP}. The latter suggests that high temperature chain branching reactions were not triggered effectively. The peak location at T_{HCP} = 1600 K was $x_s/L_I \simeq 0.25$ and shifted away from the reaction onset to $x_s/L_I \simeq 1.0$ at T_{HCP} = 1500 K. The second was attributed to turbulent mixing of the LTR fluid with the OH containing HCP resulting in a spatially distributed heat release zone. By contrast, the former case exhibited relatively thin formaldehyde layers that were quickly consumed by OH in exothermic reactions. The high temperature reactive fluid (i.e. the combined weakly and strongly reacting fluid) was only evident for T_{HCP} = 1600 K with a peak probability of ∼7.3% at $x_s/L_I \simeq 0.5$. The spatial extent was limited to 1.5 L_I, which can be attributed to dilatation. By contrast, Hampp and Lindstedt [22, 21] showed the presence of high temperature reactive fluids (i.e. distinct [OH] levels) in an ultra-lean (Φ = 0.20) DME/air flame supported at T_{HCP} = 1700 K. The comparison illustrates the importance of the external enthalpy source to the burning mode and reaction progress at low Da.

3.3 Fuel Effects on Conditional Velocity Statistics

The impact of fuel reactivity on the flow field was further analysed using conditional multi-fluid velocity statistics. The data were conditioned on the SPS and aligned at x_s = 0. The mean conditional velocities and turbulent fluctuations were normalised by the mean axial reactant fluid at the nozzle exit, see Table 5. A minimum of 75 vectors was used for the statistical analysis with a maximum change of 10% in the fluctuations within the last 20% of the sample. The reactant nozzle exit velocity was defined as negative and the counter flowing HCP as positive, see Fig. 1.

3.3.1 Conditional Reactant Fluid Velocity

The conditional mean axial reactant fluid velocities ($\overline{U_{0,r}}$ / $\overline{U_{r,NE}}$) are depicted, along with the axial ($\overline{u'_{0,r}}/\overline{U_{r,NE}}$) and radial ($\overline{v'_{0,r}}/\overline{U_{r,NE}}$) fluctuations in Fig. 6. No distinct differences were observed between the fuels for $Da \ll 1$. The impact of differences in the combustion chemistry became evident for the cases with Φ = 0.60. The higher fuel reactivity of DME promoted an advanced reaction onset and flame detachment from the stagnation plane. The mean velocity at x_s = 0 (the location of reaction onset) was in line with the natural reactant flow direction with $\overline{U_{0,r}}$ = -0.6 m s^{-1}. By contrast, $\overline{U_{0,r}} \simeq$ 0.2 m s^{-1} for EtOH and CH_4 indicating a HCP dominated reaction onset. With increasing

Da (i.e. Φ = 1.0), the reaction onset shifted further upstream towards the UN with elevated $\overline{U_{0,r}}$ = -2.4, -2.0 and -1.0 m s^{-1} for DME, EtOH and CH_4, respectively. The modest difference between DME and EtOH is consistent with the increased strain resilience of DME and thus the reduced frequency of local extinctions. The trends are also consistent with the normalised mean velocity ($\overline{u^*}/u'$) at the leading flame edge, shown in Table 5, with no fuel chemistry effect apparent for $Da \ll 1$ where $\overline{u^*} = 2.7$ as for the $\Phi = 0$ mixing layer. For the DME case at Φ = 0.60 $\overline{u^*}/u'$ increased to 2.9, while the EtOH and CH_4 remained mixing dominated with 2.7. For the stoichiometric cases, a further increase to 3.4 and 3.0 was observed for DME and EtOH. However, the reaction progress of the CH_4 remained governed by the HCP. The axial and radial reactant fluid fluctuations were reduced with increasing Φ, consistent with the gradual detachment of the reaction onset from the stagnation plane.

Reactant fluid pockets were observed at $x_s > 0$ with a probability $\leq 7\%$ due to fragmentation or three dimensional effects. The probability was independent of the mixture reactivity and fuel type [21, 45]. However, significant differences in the preferential flow alignment of these pockets were observed. For $Da > 1.0$, i.e. DME with $\Phi \geq 0.6$ and EtOH/CH_4 with Φ = 1.0, an alignment of $\overline{U_{0,r}}$ / $\overline{U_{r,NE}}$ with the natural reactant flow direction was observed. This was attributed to an interlayer that consisted of a highly exothermic fluid state (e.g. strongly reacting fluid) with distinct dilatation [21]. By contrast, the convective direction of the reactant fluid pocket was governed by turbulent mixing across the stagnation plane for $Da < 1$. Reactant fluid pockets aligned with the reactant fluid flow exhibited significantly ($> 50\%$) reduced axial and radial fluctuations.

3.3.2 Conditional Mixing Fluid Velocity

The conditional mean ($\overline{U_{0,m}}$ / $\overline{U_{r,NE}}$) and fluctuating ($\overline{u'_{0,m}}$ / $\overline{U_{r,NE}}$ and $\overline{v'_{0,m}}$ / $\overline{U_{r,NE}}$) mixing fluid velocities, see Fig. 7, were governed by the HCP momentum (i.e. positive values) and independent of the fuel reactivity for $Da \leq 1$ (i.e. DME Φ = 0.20; EtOH and CH_4 $\Phi \leq$ 0.60). By contrast, for DME at Φ = 0.60 reduced $\overline{U_{0,m}}$ / $\overline{U_{r,NE}}$ and fluctuation levels were observed. The mean axial mixing fluid velocity of the stoichiometric DME and EtOH cases were in line with the UN reactant flow direction at x_s = 0, while the CH_4 flame remained strongly affected by the HCP stream. The distinctly reduced reactivity of CH_4 led to a need for higher mixture temperatures (and HCP blending quantities) that governed $\overline{U_{0,m}}$ / $\overline{U_{r,NE}}$. Minimum HCP blending fractions of 10, 20 and 35% were estimated for the mixture temperature to exceed the auto-ignition limits for DME, EtOH and CH_4 [45].

3.3.3 Conditional Weakly Reacting Fluid Velocity

The conditional mean axial weakly reacting fluid velocities ($\overline{U_{0,w}}$ / $\overline{U_{r,NE}}$) and its axial ($\overline{u'_{0,w}}$ / $\overline{U_{r,NE}}$) and radial ($\overline{v'_{0,w}}$ / $\overline{U_{r,NE}}$) fluctuations are depicted in Fig. 8. For flames with $Da < 1$, the $\overline{U_{0,w}}$ / $\overline{U_{r,NE}}$ were nearly identical for all fuels. The $\overline{U_{0,w}}$ / $\overline{U_{r,NE}}$ of DME at Φ = 0.60 separated from the EtOH and CH_4 cases and was in line with the UN reactant flow at x_s = 0, i.e. negative values. The attenuated axial velocity fluctuations were attributed to reduced HCP blending fractions and thus enhanced dilatation. The weakly reacting fluid velocity of the stoichiometric DME and EtOH cases coincided and showed reduced fluctuation levels compared to CH_4. The delayed separation of the reaction onset from the stagnation plane, the continuous requirement for substantial HCP support and, consequently, the attenuated dilatation effect of the weakly reacting fluid for CH_4 mixtures suggests a strong influence of the fuel reactivity. The pronounced low temperature reactivity [79] of DME caused advanced dilatation that was readily apparent for $Da \simeq 1$. Overall, the trends of weakly reacting fluid velocities were similar to the mixing fluid velocities, yet the absolute values were consistently higher.

3.3.4 Conditional Strongly Reacting Fluid Velocity

Self-sustained burning was not realised for any fuel with Φ = 0.2 under the current conditions. For Φ = 0.6 the conditional strongly reacting fluid mean velocity ($\overline{U_{0,s}}$ / $\overline{U_{r,NE}}$) for DME (Da = 1.2) case was distinctly lower compared to EtOH (Da = 1.0) and CH_4 (Da = 0.44). For DME the value of $\overline{U_{0,s}}$ / $\overline{U_{r,NE}}$ was distinctly lower than the corresponding weakly reacting fluid velocity while EtOH and CH_4 flames did not show a distinct difference. The DME case further exhibited distinctly reduced (50%) axial velocity fluctuations. For the stoichiometric flames with $Da > 1$ the discrepancies between DME and EtOH vanished and similar values of $\overline{U_{0,s}}$ / $\overline{U_{r,NE}}$ were obtained due to self-sustained flames detached from the stagnation plane. The finding is consistent with the similar heat release parameters $\tau = (T_{ad} - T_r)/T_r$ = 6.1 versus 5.9 and conventional burning properties (e.g. S_L = 0.50 versus 0.46 m s^{-1}) for DME and EtOH at Φ = 1.0, respectively.

However, the likelihood of self-sustained combustion differed for DME and EtOH as shown in Fig. 4. The slightly more negative $\overline{U_{0,s}}$ / $\overline{U_{r,NE}}$ for the stoichiometric DME flame can be explained by the differences in $\overline{u*}/u'$ and more pronounced detachment of the flame from the stagnation plane. By contrast, the CH_4 flames showed a reduced detachment and were consequently subjected to a higher rate of strain as discussed below. The strongly reacting fluid velocity was accordingly more influenced by the HCP leading to reduced dilatation away from the origin (i.e. $x_s/L_I > 0.5$). This led to substantially increased axial and radial fluctuations for CH_4.

3.4 Fuel Effects at Similar Damköhler Numbers

The DME flame with Φ = 0.60 ($Da = 1.2$) and an additional CH_4 case featuring Φ = 0.80 ($Da = 1.5$) provided a comparison of two flames with similar and close-to unity Damköhler numbers. The two cases, however, featured distinctly different auto-ignition delay times (factor of $\sim$ 50) with the minimum for fresh reactants in contact with the HCP at 1700 K determined to be 9.3 and 426 μs for DME and CH_4, respectively [45]. Comparisons are shown in Figs. 10 and 11. Strong similarities in the multi-fluid probabilities and the multi-fluid conditional velocities were evident. The reactant, mixing and strongly reacting fluid probabilities agreed well. The difference in the weakly reacting fluid probability is consistent with the shorter auto-ignition delay for the DME mixture.

The mean conditional reactant fluid velocities agreed well as shown in Fig. 11. By contrast, the lower (i.e. alignment with the UN reactant flow) mixing and weakly reacting fluid velocity for DME again suggested reduced HCP blending fractions consistent with the different auto-ignition characteristics. The larger negative conditional strongly reacting fluid velocity at x_s = 0 and enhanced dilatation at $x_s > 0$ for the CH_4 flame is consistent with the higher heat release of the closer to stoichiometric flame.

3.5 Conditional Strain Distribution on Material Surfaces

The in-plane rate of strain and vorticity were calculated from the instantaneous PIV data based on Eq. (5).

$$e_{ij} = \frac{1}{2}\frac{\partial u_i}{\partial x_j} + \frac{\partial u_j}{\partial x_i} \qquad \omega_{ij} = \frac{\partial u_i}{\partial x_j} - \frac{\partial u_j}{\partial x_i} \qquad f = \mathbf{R} \cdot e \tag{5}$$

The strain rate tensor was rotated by Θ, where $\mathbf{R}$ is the rotation matrix and Θ is the angle between the iso-contour normal and the SPS. This defined the normal ($a_n = f_{11}$) and tangential ($a_t = f_{22}$) strain components that were further, along with the vorticity, conditioned on the fluid state material surfaces (β) [22]. In addition, the total rate of strain ($a_d|\beta = e_{\beta,11} + e_{\beta,22}$) is listed in Table 6. The analysis was conducted within $\pm$ L_I/2 radially away from the SPS to include the movement of the stagnation point [38].

3.5.1 Fuel Effects on Conditional Strain Distribution

Strain Distribution along the Reactant Fluid Surfaces

The normal strain evaluated along the reactant fluid iso-contour is depicted in Fig. 12. In the following, only mean values are discussed with the rms spread listed in Table 6. The mean normal compressive strain at Φ = 0.20 was fuel independent with $a_n|R$ = -1500 $\pm$ 50 s^{-1} as the reaction onset was dominated by the mixing of HCP. The fuel dependency

becomes apparent as Da increased. The mean $a_n|R$ for DME reduced by 70% from -1550 to -480 s^{-1} for $0.1 < Da < 5.1$. By contrast, the corresponding rate of strain for the methane cases ($0.1 < Da < 2.1$) reduced by 18% towards lower compressive strain, while $a_n|R$ for EtOH experienced an attenuation of 58% ($0.1 < Da < 4.4$). The reduction of the $a_n|R$ indicated a gradual detachment of the first thermal alternation iso-contour from the stagnation plane with increasing Da that was further in line with the increase in $\overline{u^*}$. At high Da, the iso-contour was anchored in regions with a relatively high axial velocity, but low compressive strain, which is characteristic for a reaction onset driven by self-sustained burning. The upstream shift of the reactant fluid material surface further resulted in reduced levels of extensive tangential strain and a strong attenuation in conditional vorticity levels of the order of 50% as listed in Table 6. By contrast, $a_n|R$ for CH_4 suggested no clear spatial separation of the reactant fluid surface from the stagnation plane. This caused a modest increase ($< 10\%$) of $a_t|R$ and a modest reduction ($\sim$13%) $\omega|R$ with increasing Φ. The earlier transition of DME and EtOH to strongly dilating fluid states, compared to CH_4, was also reflected in the total rate strain. For Φ = 0.2, $a_d|R$ = -760 $\pm$ 21 s^{-1} and was only modestly affected by the fuel reactivity. By contrast, the reactant fluid iso-contours of the stoichiometric DME and EtOH cases was situated in regions of extensive total rates of strain ($a_d|R \simeq$ 320 and 190 s^{-1} respectively), while the corresponding CH_4 iso-contour was found in compressive strain regions with $a_d|R$ = -420 s^{-1}. It can further be noticed that the DME and EtOH showed strong similarities, while CH_4 showed a broadened PDF that was attributed to a pulsating burning mode that was previously observed at reduced Re_t by Mastorakos et al. [80] amongst others. Moreover, while the DME and EtOH cases with $Da > 1$ showed a clear reduction of a_n with increasing Φ compared to the mixing cases (i.e. air with Φ = 0.0), the CH_4 cases showed strong similarities with the latter for all stoichiometries. The rates of strain conditioned upon the mixing fluid material surface showed similar trends with values listed in Table 6.

Strain Distribution along Chemically Active Fluid Surfaces

The strain distribution along the weakly reacting material surface ($a|W$) is depicted in Fig. 13. The compressive normal strain was relatively fuel and equivalence ratio independent at $Da \leq 1$ with $a_n|W$ = -1260$\pm$70 s^{-1}. At high Da (i.e. stoichiometric cases), the EtOH case showed a reduced normal compressive strain compared to DME, while CH_4 exhibited an increased compressive strain. No distinct fuel related trends were evident for the total rate of strain. However, $a_d|W$ showed a attenuated contracting strain with increasing Φ for all fuels due to increased heat release. The conditional vorticity levels were consistently similar to the values found in the proximity of the stagnation plane ($\omega|W$ = 2400$\pm$370 s^{-1}). The absence of clear fuel dependent trends suggested a strong HCP

influence with the accompanying modest heat release at high dilution ratios. This is consistent with the findings of Chakraborty and Swaminathan [81] that showed a lack of flow alignment for low Da flows with reduced heat release.

The strongly reacting fluid iso-contour was situated in low compressive strain ($a_n|S$) regions, as depicted in Fig. 14, with $a_n|S$ approximately 18% and 40% lower than the corresponding strain acting on the weakly reacting fluid for Φ = 0.6 and 1.0, respectively. The modestly higher a_n for DME compared to EtOH (i.e. -700 s^{-1} versus -420 s^{-1}) at Φ = 1.0 is consistent with the increased resilience of DME to strain [30]. Self-sustained DME flames accordingly existed in regions where EtOH flames were extinguished or relied on thermal support to a greater extent. This is also consistent with the reduced $a_n|W$ of the stoichiometric EtOH flame discussed above. The methane flame remained located in the proximity of the stagnation plane with a compressive strain of -970 s^{-1}. Overall, the mean $a_n|S$ reduced by 30, 60 and 5% with increasing Φ for DME, EtOH and CH_4.

The extensive tangential rate of strain remained approximately constant at $a_t|S$ (670 $\pm$ 66 s^{-1}) for all cases (see Table 6) as increases in dilatation were balanced by the detachment from the stagnation plane. The total rates of strain showed a shift from contracting ($a_d|S$ = -400 s^{-1}) to dilating strain (240$\pm$40 s^{-1}) with increasing Φ for DME and EtOH. A distinct reduction ($\sim$ 70%) in $a_d|S$ was evident for CH_4. The PDF spread for $a_n|S$ and $a_t|S$ at Φ = 0.6 was within 8% of weakly reacting fluid for all fuels. By contrast, the spread for the stoichiometric cases was 15% lower than that of the weakly reacting fluid. The reduction was attributed to an iso-contour governed by conventional flame propagation rather than turbulent mixing. This is consistent with the vorticity ($\omega|S$) reduction of $\sim$ 15% and $\sim$ 30% compared to $\omega|W$ at Φ = 0.6 and 1.0, respectively. The less pronounced strain reduction for the CH_4 cases was caused by the delayed onset of self-sustained flame propagation.

3.5.2 Burnt Gas Effect on Conditional Strain Distribution

The rate of strain along the reactant fluid iso-contour was only modestly affected by the T_{HCP} variation. The mean normal compressive ($a_n|R$), tangential ($a_t|R$) and total ($a_d|R$) strain and vorticity ($\omega|R$) were -1070 $\pm$ 158 s^{-1}, 419 $\pm$ 34 s^{-1}, -681 $\pm$ 100 s^{-1} and -668 $\pm$ 114 s^{-1}, respectively, with the PDF shapes maintained. A data summary is provided in Table 7.

Strain Distribution along the Low Temperature Reacting Fluid Surfaces

The conditional strain and vorticity along the low temperature reacting fluid material surface is depicted in Fig. 15. The mean values of PDF($a_n|LTR$) and PDF($a_t|LTR$) increased more than twofold from -568 $< a_n|LTR$ (s^{-1}) $<$ -1451 and 205 $< a_t|LTR$ (s^{-1})

$<$ 484 for 1200 $<$ T_{HCP} (K) $<$ 1600. The skewness of the PDFs($a_n|LTR$) towards reduced compressive strain increased with decreasing T_{HCP} with a mode shift from -1280 to -440. The spread was reduced by 22% from 1804 to 1410 s^{-1}. The PDFs($a_t|LTR$) were less skewed towards reduced extensive strains. The mean vorticity increased significantly with T_{HCP}. The elevated skewness towards reduced normal and tangential strain with lower T_{HCP} was attributed to the quenching of CH_2O in higher strain regions. At T_{HCP} = 1600 K formaldehyde was quickly consumed and appeared in relatively thin layers.

Strain Distribution along the Heat Release Fluid Surfaces

The rate of strain on the heat release surface is depicted in Fig. 16. The mean PDF ($a_n|HR$) increased twofold from -975 $<$ $a_n|HR$ (s^{-1}) $<$ -1635 with increasing T_{HCP} and exhibited a mode shift from -900 to -1560 s^{-1}. The rms increased by $\sim$ 20% with T_{HCP}. The mean tangential strain increased at a similar rate to the PDFs($a_t|LTR$), while absolute values were on average $\sim$20% higher. The latter was attributed to the enhanced dilatation. For $T_{HCP} \leq$ 1400 K the heat release fluid was found in low strain pockets within the mixing layer of the stagnation plane. The vorticity levels were $>$ 30% below corresponding reactant values. By contrast, at $T_{HCP} \geq$ 1500 K the heat release may occur in flamelet–like layers that survived elevated rates of strain. The high temperature reactive fluid was statistically relevant only for T_{HCP} = 1600 K. The mean normal compressive and tangential strains were -1975$\pm$2150 s^{-1} and 593$\pm$1390 s^{-1}, respectively.

4 Conclusions

Work performed under award FA9550-17-1-0021 has clarified a number of critical aspects associated with burning mode transitions in turbulent fuel lean to stoichiometric premixed turbulent flames. The study has included the use of DME and EtOH due to their profoundly different combustion characteristics and the need to establish the level of impact of different oxidation pathways in an unambiguous manner. The fuels are isomeric forms (CH_3-O-CH_3 and CH_3-CH_2-OH) with the same elemental composition (H_6C_2O) and effectively the same transport properties. The work has provided the basis for the introduction of increasingly complex hydrocarbons leading up to aviation fuels, such as JP-10 [19], that highlight additional chemical complexities. The probabilities of encountering multiple fluid states, conditioned on the reaction onset iso-contour, were used to quantify the impact of the combustion chemistry with a more rapid transition to chemically active fluid states and self-sustained burning evident for DME due to its lower auto-ignition temperature and higher resilience to strain. This caused the flame to be anchored in regions of higher reactant fluid velocities for Da numbers around unity. By contrast, the transition

from supported to a self-sustained flame propagation was delayed for EtOH and distinctly so for CH_4. The greater strain resilience of DME led to a slightly higher compressive strain along the iso-contours of chemically active fluid material compared to EtOH, while the further reduced reactivity of methane resulted in burning close to the stagnation plane and hence in regions characterised by high strain and vorticity levels. The results accordingly show that there is a significant influence of the type of fuel used on the transition towards distributed combustion.

The multi-fluid probabilities further show that the aligned extent of the reaction zone is typically less than two integral length scales of turbulence. Inside the reaction zone, the probability of finding intermediate fluid states (i.e. beyond bimodal statistics) was found to be strongly fuel and Da number dependent with values exceeding 90% for $Da \leq 1$. A distinct impact of the fuel reactivity and ease to ignition was also observed in the weakly reacting fluid velocities, characteristic of combustion supported by the counterflowing hot combustion products (HCP), with an advanced reaction onset and stronger pronounced dilatation observed for DME. The corresponding EtOH cases showed attenuated dilatation and a delayed reaction onset. Both phenomena were much more distinct for CH_4 and can partly be attributed to delayed auto-ignition facilitating higher HCP addition rates. A comparison at identical Lewis number for DME and EtOH, further highlights the importance of the overall combustion chemistry in turbulent reacting flows. The chemistry differences caused large changes in conditional velocity statistics and the impact was hence not subtle.

The work has further shown that increasing thermal support temperatures close to or higher than the adiabatic flame temperature gradually favoured flamelet–like structures. The latter were characterised by steep scalar gradients, thin CH_2O layers and a sequential occurrence of preheat, heat release and high temperature flame zones. Such reaction zones survived relatively high rates of strain. However, the overall likelihood remained comparatively low (i.e. $\sim$30%) under the conditions reported here. By contrast, reduced enthalpy support (lower T_{HCP}) led to a spatial distribution of low temperature reactive zones with significantly reduced species gradients and peak levels. Significant high temperature chain branching (i.e. distinct OH levels) was not observed for $T_{HCP} \leq 1400$ K. The spatially distributed heat release (cf. the cross-correlation of $CH_2O \times OH$) for thermally supported burning occurred within the HCP. In comparison to the low temperature reactive fluid, the underlying normal strain increased due to the proximity to the stagnation plane, while the increase in extensive tangential strain was attributed to dilatation. The burning mode and the reaction progress of low Da reacting flows is strongly dependent on the thermochemical state of the external enthalpy source. Consequently, the data are expected to be particularly valuable for the development and validation of numerical models that aim to delineate combustion processes that operate in the absence of distinct flame fronts and

where reaction progress may be dominated by an external enthalpy source.

In summary, it has been shown that low Damköhler numbers lead to a separation of reaction zones and flame structures that are distinctly different from those associated with burning in the flamelet regime of combustion. The work further suggests that turbulent mixing of separated reaction zones can be expected to become of significant importance and merits further investigation. It has also been shown that conventional combustion regime diagrams are inadequate, that auto-ignition based combustion may become a feature and that corresponding Damköhler number definitions are required. Autoignition based combustion regimes are dominant in augmentors, may become dominant in advanced gas turbines, due to high preheat and pressure, and are in need of further quantification.

5 References

[1] V. A. Sabelnikov, A. N. Lipatnikov, Recent Advances in Understanding of Thermal Expansion Effects in Premixed Turbulent Flames, Ann. Rev. Fluid Mech. 49 (2017), 91–117.

[2] R. W. Bilger, S. B. Pope, K. N. C. Bray, J. F. Driscoll, Paradigms in turbulent combustion research, Proc Combust. Inst. 30 (2005), 21–42.

[3] B. Savard, G. Blanquart, Effects of dissipation rate and diffusion rate of the progress variable on local fuel burning rate in premixed turbulent flames, Combust. Flame 180 (2017), 77–87.

[4] K. N. C. Bray, Laminar Flamelets and the Bray, Moss, and Libby Model, in N. Swaminathan, K. N. C. Bray (Eds.), Turbulent Premixed Flames, Cambridge University Press, 2011, 41–60, ISBN: 978-0-521-76961-7.

[5] F. E. Marble, J. E. Broadwell, The coherent flame model for turbulent chemical reactions, Project Squid, Tech. Rep. (1977), TRW-9-PU.

[6] F. A. Williams, Turbulent combustion, in J. D. Buckmaster (Ed.), The Mathematics of Combustion, SIAM, Philadelphia (1985), 97–131, ISBN: 978-0-89871-053-3.

[7] T. Plessing, N. Peters, J. G. Wünning, Laseroptical investigation of highly preheated combustion with strong exhaust gas recirculation, Proc. Combust. Inst. 27 (1998), 3197–3204.

[8] F. J. Weinberg, Combustion temperatures: The future?, Nature 233 (1971), pp. 239–241.

[9] V. D. Milosavljevic, R. P. Lindstedt, M. D. Cornwell, E. J. Gutmark, E. M. Váos, Combustion Instabilities Near the Lean Extinction Limit, in G. Roy, K. H. Yu, J. H. Whitelaw, J. J. Witton (Eds.), Advances in Combustion and Noise Control, Cranfield University Press, 2006, 149–165.

[10] J. A. Wünning, J. G. Wünning, Flameless oxidation to reduce thermal NO-formation, Prog. Energ. Combust. 23 (1997), 81–94.

[11] Y. Minamoto, N. Swaminathan, R. S. Cant, T. Leung, Reaction Zones and Their Structure in MILD Combustion, Combust. Sci. Technol. 186 (2014) 1075–1096.

[12] B. Zhou, C. Brackmann, Q. Li, Z. Wang, P. Petersson, Z. Li, M. Aldén, X.-S. Bai, Distributed reactions in highly turbulent premixed methane/air flames. Part I. Flame structure characterization, Combust. Flame 162 (2015), 2937–2953.

[13] M. de Joannon, P. Sabia, G. Sorrentino, A. Cavaliere, Numerical study of mild combustion in hot diluted diffusion ignition (HDDI) regime, Proc Combust. Inst. 32 (2009), 2147–3154.

[14] H. Carlsson, R. Yu, X.-S. Bai, Flame structure analysis for categorization of lean premixed CH4/air and H2/air flames at high Karlovitz numbers: Direct numerical simulation studies, Proc Combust. Inst. 35 (2015), 1425–1432.

[15] C. Duwig, B. Li, Z. S. Li, M. Aldén, High resolution imaging of flameless and distributed turbulent combustion, Combust. Flame 159 (2012), 306–316.

[16] B. Zhou, C. Brackmann, Z. Li, M. Aldén, X.-S. Bai, Simultaneous multi-species and temperature visualization of premixed flames in the distributed reaction zone regime, Proc. Combust. Inst. 35 (2015), 1409–1416.

[17] B. Zhou, Q. Li, Y. He, P. Petersson, Z. Li, M. Aldén, X.-S. Bai, Visualization of multi-regime turbulent combustion in swirl-stabilized lean premixed flames, Combust. Flame 162 (2015), 2954–2958.

[18] B. Zhou, C. Brackmann, Z. Wang, Z. Li, M. Richter, M. Aldén, X.-S. Bai, Thin reaction zone and distributed reaction zone regimes in turbulent premixed methane/air flames: Scalar distributions and correlations, Combust. Flame (2016), http://dx.doi.org/10.1016/j.combustflame.2016.06.016.

[19] K. H. H. Goh, P. Geipel, F. Hampp, R. P. Lindstedt, Regime transition from premixed to flameless oxidation in turbulent JP-10 flames, Proc. Combust. Inst. 34, (2013), 3311–3318.

[20] K. H. H. Goh, P. Geipel, R. P. Lindstedt, Turbulent transport in premixed flames approaching extinction, Proc. Combust. Inst. 35 (2015), 1469–1476.

[21] F. Hampp, R. P. Lindstedt, Quantification of combustion regime transitions in premixed turbulent DME flames, Combust. Flame 182 (2017), 248–268.

[22] F. Hampp, R. P. Lindstedt, Strain distribution on material surfaces during combustion regime transitions, Proc. Combust. Inst. 36 (2017), 1911–1918.

[23] F. Hampp, R. P. Lindstedt, Quantification of external enthalpy-controlled combustion at unity Damköhler number, in A. K. Runchal, A. K. Gupta, A. Kushari, A. De Suresh, K. Aggarwal (eds.) Energy for Propulsion A Sustainable Technologies Approach, Springer Nature Singapore Pte Ltd., (2018), ISBN:978-981-10-7472-1.

[24] F. Hampp, S. Shariatmadar, R. P. Lindstedt, Quantification of low Damköhler number turbulent premixed flames, Proc. Combust. Inst. 37 (2019) 2373-2381.

[25] M. de Joannon, G. Langella, F. Beretta, A. Cavaliere, C. Noviello, Mild Combustion: Process Features and Technological Constrains, Combust. Sci. Technol. 153 (2000), 33–50.

[26] P. Sabia, M. de Joannon, M. L. Lavadera, P. Giudicianni, R. Ragucci, Autoignition delay times of propane mixtures under MILD conditions at atmospheric pressure, Combust. Flame 161 (2014), 3022–3030.

[27] P. Sabia, M. de Joannon, G. Sorrentino, P. Giudicianni, R. Ragucci, Effects of mixture composition, dilution level and pressure on auto-ignition delay times of propane mixtures, Chem. Eng. J. 277 (2015), 324–333.

[28] J. Ye, P. R. Medwell, E. Varea, S. Kruse, B. B. Dally, H. G. Pitsch, An experimental study on MILD combustion of prevaporised liquid fuels, Appl. Energ. 151, 93–101.

[29] Z. Chen, X. Qin, Y. Ju, Z. Zhao, M. Chaos, F. L. Dryer, High temperature ignition and combustion enhancement by dimethyl ether addition to methane-air mixtures, Proc Combust. Inst. 31 (2007), 1215–1222.

[30] Y. L. Wang, P. S. Veloo, F. N. Egolfopoulos, T. T. Tsotsis, A comparative study on the extinction characteristics of non-premixed dimethyl ether and ethanol flames, Proc Combust. Inst. 33 (2011), pp.1003–1010.

[31] Y. L. Wang, An experimental and numerical investigation of fundamental combustion properties of biofuels, PhD thesis, University of Southern California, August 2011, url: uscthesesreloadpub_Volume71/etd-WangYangLe-256.pdf.

[32] F. Hampp, R.P. Lindstedt, Quantification of fuel chemistry effects on burning modes in turbulent premixed flames, Submitted to Combust. Flame, Revised February 2020.

[33] C. Arcoumanis, C. Bae, R. Crookes, E. Kinoshita, The potential of di-methyl ether (DME) as an alternative fuel for compression-ignition engines: A review, Fuel 87 (2008), 1014–1030.

[34] P. Allison, Y. Chen, J. F. Driscoll, Investigation of Dimethyl Ether Combustion Instabilities in a Partially-Premixed Gas Turbine Model Combustor Using High-Speed Laser Diagnostics, AIAA 52 (2014), DOI: 10.2514/6.2014-0660.

[35] K. Kohse-Höinghaus, P. Oßwald, T. A. Cool, T. Kasper, N. Hansen, F. Qi, C. K. Westbrook, P. R. Westmoreland, Biofuel Combustion Chemistry: From Ethanol to Biodiesel, Angew. Chem. Int. Ed. 49 (2010), 3572–3597.

[36] S.-W. Park, Detailed Chemical Kinetic Model for Oxygenated Fuels, PhD thesis, Imperial College, March 2012, url: http://hdl.handle.net/10044/1/9599.

[37] F. Hampp, R. P. Lindstedt, Fractal Grid Generated Turbulence - A Bridge to Practical Combustion Applications, in Y. Sakai and C. Vassilicos (eds.) Fractal Flow Design: How to Design Bespoke Turbulence and why, Springer-Verlag, CISM Int. Mech. Sci. 568, 2016, DOI:10.1007/978-3-319-33310-6 3.

[38] P. Geipel, K. H. H. Goh, R. P. Lindstedt, Fractal-Generated Turbulence in Opposed Jet Flows, Flow Turbul. Combust. 85 (2010), 397–419.

[39] B. Böhm, O. Stein, A. Kempf, A. Dreizler, In-Nozzle Measurements of a Turbulent Opposed Jet using PIV, Flow Turbul. Combust. 85 (2010), 73–93.

[40] K. H. H. Goh, Investigation of Conditional Statistics in Premixed Combustion and the Transition to Flameless Oxidation in Turbulent Opposed Jets, PhD thesis, Imperial College, Aug 2013, url: http://hdl.handle.net/10044/1/28073.

[41] K. H. H. Goh, P. Geipel, R. P. Lindstedt, Lean premixed opposed jet flames in fractal grid generated multiscale turbulence, Combust. Flame 161 (2014), 2419–2434.

[42] D. Geyer, A. Kempf, A. Dreizler, J. Janicka, Turbulent opposed-jet flames: A critical benchmark experiment for combustion LES, Combust. Flame 143 (2005), 524–548.

[43] K. H. H. Goh, P. Geipel, F. Hampp, R. P. Lindstedt, Flames in fractal grid generated turbulence, Fluid Dyn. Res. 45, (2013), 061403.

[44] G. Coppola, A. Gomez, Experimental investigation on a turbulence generation system with high-blockage plates, Exp. Therm. Fluid Sci. 33 (2009), 1037–1048.

[45] F. Hampp, Quantification of Combustion Regime Transitions, PhD thesis, Imperial College, May 2016, url: http://hdl.handle.net/10044/1/32582.

[46] J. Kerl, T. Sponfeldner, F. Beyrau, An external Raman laser for combustion diagnostics, Combust. Flame 158 (2011), 1905-–1907.

[47] S. A. Skeen, J. Manin, L. M. Pickett, Simultaneous formaldehyde PLIF and high-speed schlieren imaging for ignition visualization in high-pressure spray flames, Proc. Combust. Inst. 35 (2015) 3167–3174.

[48] B. Wieneke, K. Pfeiffer, Adaptive PIV with variable interrogation window size and shape, 15^{th} Int. Symp. Appl. Laser Tech. Fluid Mech. (2010), url: http://ltces.dem.ist.utl.pt/LXLASER/lxlaser2010/upload/1845_qkuqls_1.12.3.Full_1845.pdf.

[49] B. Coriton, J. H. Frank, A. Gomez, Effects of strain rate, turbulence, reactant stoichiometry and heat losses on the interaction of turbulent premixed flames with stoichiometric counterflowing combustion products, Combust. Flame 160 (2013), 2442–2456.

[50] M. P. Burke, M. Chaos, Y. Ju, F. L. Dryer, S. J. Klippenstein, Comprehensive H_2/O_2 kinetic model for high-pressure combustion, Int. J. Chem. Kinet., 44 (2012), 444–474.

[51] Y. L. Wang, A. T. Holley, C. Ji, F. N. Egolfopoulos, T. T. Tsotsis, H. J. Curran, Propagation and extinction of premixed dimethyl-ether/air flames, Proc. Combust. Inst. 32 (2009), 1035–1042.

[52] X. Qin, Y. Ju, Measurements of burning velocities of dimethyl ether and air premixed flames at elevated pressures, Proc. Combust. Inst. 30 (2005), 233–240.

[53] J. de Vries, W. B. Lowry, Z. Serinyel, H. J. Curran, E. L. Petersen, Laminar flame speed measurements of dimethyl ether in air at pressures up to 10 atm, Fuel, 90 (2011), 331–338.

[54] T. A. Cool, J. Wang, N. Hansen, P. R. Westmoreland, F. L. Dryer, Z. Zhao, A. Kazakov, T. Kasper, K. Kohse-Höinghaus, Photoionization mass spectrometry and modeling studies of the chemistry of fuel-rich dimethyl ether flames, Proc. Combust. Inst. 31 (2007), 285–293.

[55] J. Wang, M. Chaos, B. Yang, T. A. Cool, F. L. Dryer, T. Kasper, N. Hansen, P. Oßwald, K. Kohse-Höinghaus, P. R. Westmoreland, Composition of reaction intermediates for stoichiometric and fuel-rich dimethyl ether flames: flame-sampling mass spectrometry and modeling studies, Phys. Chem. Chem. Phys. 11 (2009), 1328–1339.

[56] C. K. Law, D. L. Zhu, G. Yu, Propagation and extinction of stretched premixed flames, Proc. Combust. Inst. 21 (1986), 1419–1426.

[57] W. P. Jones, R. P. Lindstedt, The Calculation of the Structure of Laminar Counterflow Diffusion Flames Using a Global Reaction Mechanism, Combust. Sci. Techn. 61 (1988), 31–49.

[58] N. Peters, Kinetic foundation of thermal flame theory, in W. A. Sirignano, A. G. Merzhanov, L. de Luca (Eds.), Advances in Combustion Science: In Honor of Y. B. Zel'dovich, Prog. Astronautics and Aeronautics 173 (1997) 73–91.

[59] J. F. Driscoll, Turbulent premixed combustion: Flamelet structure and its effect on turbulent burning velocities, Prog. Energy Combust. Sci. 34 (2008) pp. 91–134.

[60] C. Ji, C. Liang, Y. Zhu, X. Liu, B. Gao, Investigation on idle performance of a spark-ignited ethanol engine with dimethyl ether addition. Fuel Proc. Technol. 94 (2012), 94–100.

[61] C. K. Westbrook, M. Sjöberg, N. P. Cernansky, A new chemical kinetic method of determining RON and MON values for single component and multicomponent mixtures of engine fuels, Combust Flame 195 (2018), 50–62.

[62] J. Kubesh, S. R. King, W. E. Liss, Effect of gas composition on octane number of natural gas fuels, SAE Technical Paper (1992), 922359.

[63] M. Naito, C. Radcliffe, Y. Wada, T. Hoshino, X. Liu, M. Arai, M. Tamura, A comparative study on the autoxidation of dimethyl ether (DME) comparison with diethyl ether (DEE) and diisopropyl ether (DIPE), J. Loss Prev. Proc. Ind. 18 (2005) 469–473.

[64] C.-C. Chen, H.-J. Liaw, C.-M. Shu, Y.-C. Hsieh, Autoignition Temperature Data for Methanol, Ethanol, Propanol, 2-Butanol, 1-Butanol, and 2-Methyl-2,4-pentanediol, J. Chem. Eng. Data 55 (2010) 5059–5064.

[65] C. Robinson, D. B. Smith, The auto-ignition temperature of methane, J. Hazard. Mat. 8 (1984) 199–203.

[66] I. G. Shepherd, R. K. Cheng, P. J. Goix, The spatial scalar structure of premixed turbulent stagnation point flames, Proc. Combust. Inst. 23 (1991), 781–787.

[67] A. M. Steinberg, J. F. Driscoll, S. L. Ceccio, Measurements of turbulent premixed flame dynamics using cinema stereoscopic PIV, Exp. Fluids 44 (2008), 985–999.

[68] B. E. Battles, R. K. Hanson, Laser-induced fluorescence measurements of NO and OH mole fraction in fuel-lean, high-pressure (1–10 atm) methane flames: Fluorescence modeling and experimental validation, J. Quant. Spectrosc. Radiat. Transfer 54 (1995), 521–537.

[69] B. Böhm, C. Heeger, I. Boxx, W. Meier, A. Dreizler, Time-resolved conditional flow field statistics in extinguishing turbulent opposed jet flames using simultaneous high-speed PIV/OH-PLIF, Proc. Combust. Inst. 32 (2009), 1647–1654.

[70] R. L. Gordon, A. R. Masri, E. Mastorakos, Simultaneous Rayleigh temperature, OH- and CH_2O–LIF imaging of methane jets in a vitiated coflow, Combust. Flame 155 (2008) 181–195.

[71] R. L. Gordon, A. R. Masri, E. Mastorakos, Heat release rate as represented by [OH] X [CH_2O] and its role in autoignition, Combust. Theor. Model. 13 (2009) 645–670.

[72] H. Shariatmadar, F. Hampp, R.P. Lindstedt, Quantification of PAH concentrations in premixed turbulent flames crossing the soot inception limit, Accepted for oral presentation at 38th Internat. Symp. on Combust., Adelaide, Australia, July 2020.

[73] H. Wang, R. Xu, K. Wang, C.T. Bowman, R.K. Hanson, D.F. Davidson. K. Brezinsky. F.N. Egolfopoulos, A physics-based approach to modeling real-fuel combustion chemistry - I. Evidence from experiments, and thermodynamic, chemical kinetic and statistical considerations, Combust. Flame 93 (2018) 502 – 519.

[74] K. A. Buch, W. J. A. Dahm, Experimental study of the fine-scale structure of conserved scalar mixing in turbulent shear flows. Part 2. Sc = 1, J. Fluid Mech. 364 (1998) 1–29.

[75] G. K. Batchelor, Small-scale variation of convected quantities like temperature in turbulent fluid Part 1. General discussion and the case of small conductivity, J. Fluid Mech. 5 (1959) 113–133.

[76] I. G. Shepherd, J. B. Moss, K. N. C. Bray, Turbulent transport in a confined premixed flame, Proc. Combust. Inst. 19 (1982) 423–431.

[77] C. J. Lawn, R. W. Schefer, Scaling of premixed turbulent flames in the corrugated regime, Combust. Flame 146 (2006) 180–199.

[78] H. Shen, J. A. Sutton, A Comparison of the Reactive OH Layer Structure between CH4- and DME-Based Turbulent Non-premixed Jet Flames, 8th National Combustion Meeting, Park City, Utah, May 2013.

[79] F. Herrmann, B. Jochim, P. Oßwald, L.Cai, H. Pitsch, K. Kohse-Höinghaus, Experimental and numerical low-temperature oxidation study of ethanol and dimethyl ether, Combust. Flame 161 (2014) 384–397.

[80] E. Mastorakos, A. M. K. P. Taylor, J. H. Whitelaw, Extinction of Turbulent Counterflow Flames with Reactants Diluted by Hot Products, Combust. Flame 102 (1995), 101–114.

[81] N. Chakraborty, N. Swaminathan, Influence of the Damköhler number on turbulence-scalar interaction in premixed flames. I. Physical insight, Phys. Fluids 19 (2007), 045103.

6 Nomenclature

Roman Letters

a	Rate of strain [s^{-1}].
$\overline{c}$	Reaction progress variable [–].
c	Progress variable; Instantaneous conditioning variable [–].
D	Burner nozzle diameter [m].
Da	Conventional Damköhler number [–].
Da_{ai}	Turbulent auto–ignition Damköhler number [–].
$d_{p,x}$	Al_2O_3 particle diameter x% [m].
e	Strain rate tensor [s^{-1}].
f	Rotated strain rate tensor [s^{-1}].
H	Burner nozzle separation [m].
I	Experimental fluorescence signal intensities [–].
$I^{\ddagger}$	Reference signal intensity [–].
Ka	Conventional Karlovitz number [–].
[k]	Theoretical concentration of species k [mol m^{-3}].
L_η	Kolmogorov length scale [m].
L_λ	Taylor microscale [m].
L_I	Integral length scale of turbulence [m].
M	Mixing fluid material surface [–].
N	Total number of images [–].
n	Instantaneous image [–].
$\hat{\mathbf{n}}$	Unit vector of the iso-contour normal [–].
$\dot{Q}$	Heat release rate [W m^{-3}].
Re	Reynolds number [–].
Re_λ	Reynolds number based on Taylor scales [–].
Re_t	Turbulent Reynolds number [–].
R	Reactant fluid material surface [–].
$\mathbf{R}$	Rotation matrix [–].
S	Strongly reacting fluid material surface [–].
S_L	Laminar burning velocity [m s^{-1}].
$\hat{\mathbf{s}}$	Unit vector of the streamline tangent [–].
T	Temperature [K].
T_{ad}	Adiabatic flame temperature [K].
T_{ai}	Auto–ignition temperature [K].
T_{HCP}	Hot combustion product temperature [K].
T_r	Reactant temperature [K].
U	Flow velocity [m s^{-1}].
$\overline{U}$	Mean unconditional axial velocity [m s^{-1}].
$\overline{U}_{...}$	Mean conditional axial velocity [m s^{-1}].
u	Axial velocity component [m s^{-1}].
$\overline{u^*}$	Leading edge velocity [m s^{-1}].
$\sqrt{u'^2}$	Unconditional axial velocity fluctuation [m s^{-1}].
$\sqrt{u'^2_{...}}$	Conditional axial velocity fluctuation [m s^{-1}].
u_{rms}	Root mean square velocity fluctuation [m s^{-1}].
$\dot{V}_{...}$	Volumetric flow rate [m^3 s^{-1}].
v	Radial velocity component [m s^{-1}].
$\sqrt{v'^2}$	Unconditional radial velocity fluctuation [m s^{-1}].

$\sqrt{\overline{v'^2_{\cdots}}}$	Conditional radial velocity fluctuation [m s^{-1}].
W	Weakly reacting fluid material surface [–].
x	Axial coordinate [m].
x_s	Distance from origin of first thermal alteration [m].
y	Radial coordinate [m].

Greek Letters

β	Material surface iso-contour [–].
δ_f	Laminar fuel consumption layer thickness [m].
δ_l	Distance between the flame edge and the stagnation plane [m].
ε_r	Rate of dissipation in the reactants [m^2 s^{-3}].
Λ	Threshold value [–].
λ_B	Batchelor scale [m].
λ_D	Mean scalar dissipation layer thickness [m].
λ_{MF}	Multi–fluid spatial resolution [m].
λ_{PIV}	PIV spatial resolution [m].
ν_r	Reactants kinematic viscosity [m^2 s^{-1}].
Φ	Equivalence ratio [–].
Θ	Angle of rotation [$^\circ$].
τ_c	Chemical timescale [s].
τ_η	Kolmogorov timescale [s].
τ_{ai}	Auto–ignition delay time [s].
τ_I	Integral timescale of turbulence [s].
ω	Vorticity [s^{-1}].

Subscripts

0	Alignment at the origin; Initial value.
Φ	Dependency on equivalence ratio.
$\ddagger$	Reference value.
BTB	Back–to–burnt configuration.
b	Bulk flow motion.
d	Total.
FS	Fluid state.
I	Integral scale; Turbulent.
HCP	Hot combustion products.
i, j	Pixel index.
k	Velocity component.
LN	Lower nozzle.
m	Mixing fluid.
NE	Nozzle exit.
n	Instantaneous image; Normal component.
p	Product fluid.
q	Extinction conditions.
r	Reactant fluid.
s	Strongly reacting (flamelet) fluid.
T	Turbulent.
t	Tangential component.
UN	Upper nozzle.
w	Weakly reacting fluid.

7 Tables

Tab. 1: Experimental Conditions for the upper nozzle fuel and equivalence ratio variation. FBA – Flash Back Arrestor, FSM – Flame Stabilising Mesh; Dil. – Dilution; NL – Nozzle Length; Cross Fractal Grid (CFG) [22]. $\dot{V}$ is the volumetric flow rate, U_b is the bulk velocity, T_r is the reactant temperature and Re and Re_t are the bulk and turbulent Reynolds number.

UN Conditions Unburnt Reactants		LN Conditions Hot Combustion Products	
$\dot{V}_{UN}$	7.07×10^{-3} m^3 s^{-1} (293 K)	$\dot{V}_{LN}$	3.10×10^{-3} m^3 s^{-1} (293 K)
$U_{b,UN}$	11.2 m s^{-1} (320 K)	$U_{b,LN}$	24.0 m s^{-1} (1700 K)
Fuel	DME, EtOH, CH_4	Fuel	H_2
Φ_{UN}	0.0 – 1.0	Φ_{LN}	1.0
T_r	320 K	T_{LN}	1700 K
Grid	CFG	Grid	FBA and FSM
NL	50 mm	NL	100 mm
Re	$\sim$ 19,550	Dil.	22% by volume of CO_2
Re_t	$\sim$ 361		

Tab. 2: Lower nozzle conditions for the T_{HCP} variation with the reactant mole fractions (X) (the missing percentile accounts for air), heat loss (HL) to the burner, equilibrium OH concentration at the nozzle exit ($[OH]_T^{\ddagger}$) and HCP bulk velocity at the nozzle exit (U_{HCP}) and T_0 = 310 K.

$T_{HCP} \times 10^3$	[K]	1.20	1.30	1.40	1.50	1.60
Φ	–	0.30	0.38	0.43	0.51	0.62
$X(H_2) \times 10^{-2}$	–	8.8	9.7	7.6	6.9	6.7
$X(CH_4) \times 10^{-2}$	–	0.61	1.1	2.2	3.1	4.1
HL	[%]	7.2	8.7	9.2	9.3	8.9
$[OH]_T^{\ddagger} \times 10^{-3}$	[mol m^{-3}]	7.38	8.40	8.89	9.72	10.8
U_{HCP}	[m s^{-1}]	22.7	23.4	24.1	24.6	25.1

Tab. 3: Comparison of calculated and experimental extinction points at Φ = 0.8 and 1.0. DME and EtOH extinction points were determined in a back to inert gas geometry [31] and the CH_4 flames in a twin geometry [56].

Fuel		DME		EtOH		CH_4	
Φ	–	0.80	1.0	0.80	1.0	0.80	1.0
Calc. a_q	s^{-1}	550	1000	350	780	1300	1700
Exp. a_q	s^{-1}	515	950	365	770	1230	1680

Tab. 4: Twin flame extinction point conditions for premixed fuel/air twin flames, where a_q is the extinction strain, T_q the peak temperature at the extinction point, $[OH]_q/[OH]^{\ddagger}$ is the normalised peak OH concentration at extinction and $\int \dot{Q}_q$ is the integrated heat release rate at the extinction point.

Fuel		DME		EtOH		CH_4	
Φ	–	0.60	1.0	0.60	1.0	0.60	1.0
a_q	s^{-1}	600	3100	500	2600	600	2000
T_q	K	1555	1760	1524	1753	1554	1879
$[OH]_q/[OH]^{\ddagger}$	–	3.5	5.8	3.0	5.4	3.2	4.5
$\int \dot{Q}_q$	MW m^{-2}	0.28	0.81	0.32	0.74	0.25	0.65

Tab. 5: Summary of turbulent and chemical conditions to derive the turbulent Reynolds, Damköhler and Karlovitz numbers for DME, EtOH and CH_4 at varying Φ and low strain rate (a = 75 s^{-1}). Φ is the equivalence ratio, S_L is the laminar burning velocity, δ_f is the laminar flame thickness, T_{ad} is the adiabatic flame temperature, τ_c is the chemical timescale, ν_r is the kinematic viscosity, Sc is the Schmidt number, u' is the axial velocity fluctuation and $\overline{U_{r,NE}}$ is the mean axial reactant velocity 1 mm away from the UN exit, u_{rms} is the rms velocity fluctuation, L_I and L_η are the integral and Kolmogorov length scale of turbulence, τ_I and τ_η are the integral and Kolmogorov timescale, u^* is the mean velocity at the leading edge, Re_t the turbulent Reynolds number, Da the Damköhler number and Ka the Karlovitz number. The reactant temperature was T_r = 320 K and the turbulence conditions were evaluated within the reactants.

Fuel	–	DME			EtOH			CH_4			Air
Φ	–	0.20	0.60	1.0	0.20	0.60	1.0	0.20	0.60	1.0	0.0
S_L	m s^{-1}	0.04	0.21	0.50	0.04	0.17	0.46	0.04	0.15	0.39	–
δ_f	mm	1.3	0.46	0.24	1.4	0.55	0.26	1.7	0.85	0.44	–
T_{ad}/T_r	–	2.8	5.5	7.2	2.8	5.5	7.2	2.7	5.3	7.0	–
τ_c	ms	33	2.2	0.48	36	2.9	0.57	41	5.7	1.1	–
$\nu_r \times 10^6$	m^2 s^{-1}	17.5	17.0	16.5	17.5	17.0	16.5	17.8	17.9	18.0	17.9
Sc	–	0.72	0.73	0.73	0.72	0.73	0.73	0.74	0.76	0.78	0.72
u'	m s^{-1}	1.7	1.8	1.7	1.6	1.6	1.9	1.9	1.9	1.9	1.7
$\overline{U_{r,NE}}$	m s^{-1}	9.3	10	10	9.8	9.5	10	9.3	9.3	9.1	10
u_{rms}	m s^{-1}					1.6					
L_I	mm					3.9 ± 0.2					
τ_I	ms					2.4					
L_η	μm					48					
τ_η	μs					135 ± 2					
$\overline{u^*}/u'$	–	2.7	2.9	3.4	2.7	2.7	3.0	2.7	2.7	2.7	2.7
δ_l/L_I	–	0.42	0.86	1.0	0.17	0.50	0.93	0.23	0.33	0.70	0.23
Re_t	–	357	367	378	356	367	378	351	349	347	349
Da	–	0.08	1.2	5.1	0.08	1.0	4.4	0.06	0.44	2.1	–
Ka	–	244	16	3.7	255	22	4.3	300	42	8.0	–

Tab. 6: Summary of normal (a_n), tangential (a_t) and total (a_d) strain as well as vorticity (ω) conditioned upon the material surfaces (β) for non-reacting (Air) and combusting mixtures of DME, EtOH and CH_4 at varying Φ. Listed is the mean and spread of the respective PDFs. R – reactants; M – mixing; W – weakly reacting; S – strongly reacting fluid.

β	Fuel	Φ	Mean				Spread (rms)			
			a_n	a_t	a_d	ω	a_n	a_t	a_d	ω
R	Air	0.0	-1550	1040	-780	2810	1170	1040	1000	1790
R	DME	0.2	-1530	830	-760	2740	1170	1020	950	1740
R	EtOH	0.2	-1450	1150	-730	2850	1170	1200	950	2010
R	CH_4	0.2	-1450	560	-760	2550	1750	1170	1240	2650
R	DME	0.6	-1190	780	-480	2270	1020	870	890	1580
R	EtOH	0.6	-1290	1050	-650	2520	1110	1150	920	1990
R	CH_4	0.6	-1370	570	-650	2470	1740	1130	1230	2650
R	DME	1	-480	720	320	1390	880	640	810	1300
R	EtOH	1	-610	680	190	1460	1020	710	920	1540
R	CH_4	1	-1190	600	-420	2230	1660	1050	1360	2450
M	Air	0.0	-1490	830	-670	2670	1250	1030	1070	1840
M	DME	0.2	-1740	890	-850	3030	1280	1120	990	1850
M	EtOH	0.2	-1470	890	-690	2740	1220	1120	990	1970
M	CH_4	0.2	-1490	660	-750	2670	1710	1260	1300	2640
M	DME	0.6	-1340	870	-520	2530	1140	980	960	1710
M	EtOH	0.6	-1410	900	-570	2620	1210	1060	1000	1960
M	CH_4	0.6	-1620	660	-750	1840	1820	1200	1290	2700
M	DME	1	-610	710	430	1510	1050	690	940	1560
M	EtOH	1	-560	770	90	1580	1100	870	990	1770
M	CH_4	1	-1620	670	-730	2860	1940	1200	1510	2750
W	DME	0.2	-1290	560	-870	2430	1030	970	940	1660
W	EtOH	0.2	-1240	830	-670	2590	1090	1020	970	1850
W	CH_4	0.2	-1370	610	-870	2850	1440	1260	1340	2450
W	DME	0.6	-1200	690	-560	2310	1020	910	930	1540
W	EtOH	0.6	-1250	1130	-570	2870	1140	1180	970	2020
W	CH_4	0.6	-1190	530	-630	2420	1480	1170	1140	2450
W	DME	1	-1150	1030	-220	2480	1160	780	1050	1660
W	EtOH	1	-820	820	40	1940	1130	900	1060	1800
W	CH_4	1	-1430	530	-710	2730	1500	1120	1260	2310
S	DME	0.6	-990	610	-400	2000	980	870	950	1520
S	EtOH	0.6	-1030	790	-400	2290	1160	1080	1010	1990
S	CH_4	0.6	-1030	570	-450	2230	1430	1160	1150	2410
S	DME	1	-700	830	180	1770	1020	680	1000	1440
S	EtOH	1	-420	570	240	1220	900	710	930	1420
S	CH_4	1	-970	570	-140	2080	1390	1000	1220	2140

Tab. 7: Summary of the normal (a_n), tangential (a_t) and total (a_d) strain and vorticity (ω) conditioned upon the material surfaces (β) for DME/air mixtures at Φ = 0.5, Re_t = 350 and Da = 0.29 for a HCP temperature variation in the range $1200 < T_{HCP}$ (K) < 1600. Listed are the mode, mean and spread of the respective PDFs. R – reactants; LTR – low temperature reactive; HR – heat release (i.e. CH_2O – OH cross-correlation); HTR – high temperature reactive; HCP – hot combustion product fluid iso-contour.

T_{HCP}	β	Mode				Mean				Spread (rms)			
		a_n	a_t	a_d	ω	a_n	a_t	a_d	ω	a_n	a_t	a_d	ω
1200	R	-640	210	-740	10	-1119	467	-708	-763	1783	1507	1729	3391
1300	R	-840	230	-840	-190	-1338	514	-771	-1058	1873	1528	1714	3476
1400	R	-830	290	-870	-550	-1544	576	-881	-1355	2149	1641	1792	3972
1500	R	-590	200	-590	-630	-1284	506	-753	-1174	1965	1565	1812	3669
1600	R	-780	360	-840	-500	-1407	500	-788	-1019	1959	1504	1625	3718
1200	LTR	-300	50	-520	0	-635	262	-460	-393	1481	1373	1434	3157
1300	LTR	-720	200	-730	-210	-1107	440	-681	-771	1735	1437	1556	3284
1400	LTR	-880	300	-890	-670	-1456	533	-876	-1061	1970	1566	1692	3482
1500	LTR	-600	210	-680	-770	-1381	530	-803	-1187	1969	1584	1821	3489
1600	LTR	-1310	590	-900	-660	-2089	788	-1003	-1923	2249	1689	1880	4284
1200	HR	-510	100	-760	0	-778	338	-593	-384	1488	1404	1443	3097
1300	HR	-890	250	-820	-90	-1070	389	-684	-244	1243	1162	1323	1515
1400	HR	-1290	370	-1130	-430	-1794	642	-1223	-619	1668	1555	1530	1908
1500	HR	-1730	560	-1180	-930	-2241	773	-1315	-1587	2030	1742	2089	2810
1600	HR	-1990	770	-1330	-920	-2582	937	-1398	-2159	2150	1799	2006	3640
1600	HTR	-2080	1090	-1300	-2330	-1975	593	-872	-2629	2530	1390	2111	2419
1200	HCP	-1100	450	-740	20	-1289	568	-809	-186	1641	1358	1849	2154
1300	HCP	-1290	580	-890	-90	-1488	630	-905	-285	1500	1216	1734	1351
1400	HCP	-1470	650	-1280	-380	-1972	724	-1349	-702	1854	1538	1870	1600
1500	HCP	-1780	630	-1190	-1000	-2344	780	-1433	-1550	2118	1721	2194	2440
1600	HCP	-1820	530	-1400	-600	-2308	769	-1451	-1234	2000	1706	1911	2454

8 Figures

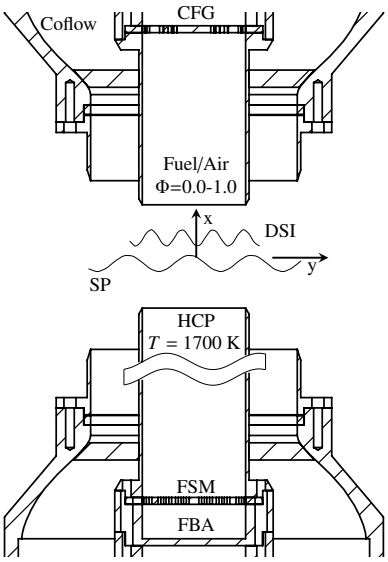

Fig. 1: Schematic of experimental configuration. Unreacted premixed fuel/air is introduced in the upper nozzle (UN) stabilised by hot combustion products (HCP) from a stoichiometric H_2/CO_2/air flame in the lower nozzle (LN). CFG – Cross Fractal Grid, FBA – Flash Back Arrestor, FSM – Flame Stabilising Mesh.

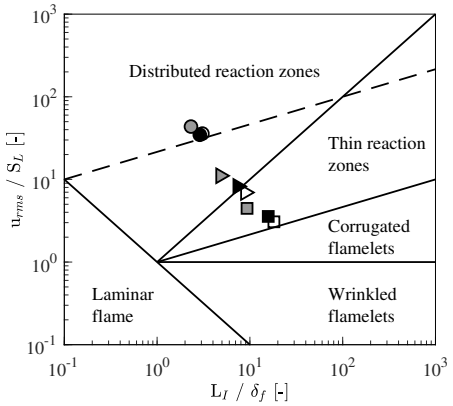

Fig. 2: Combustion regime transitions of DME, EtOH and CH_4 visualised in a Borghi diagram for varying Φ. Empty symbols are the DME cases, filled EtOH and grey CH_4. ○: Φ = 0.2, ▷: Φ = 0.6, □: Φ = 1.0.

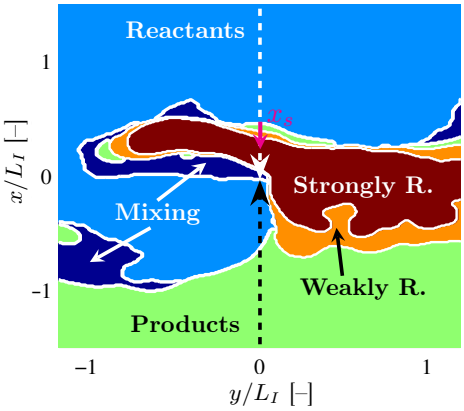

Fig. 3: Instantaneous quinary multi-fluid field for DME / air at Φ = 0.60 with T_{HCP} = 1700 K truncated around the stagnation point. Vertical white/black arrows show the theoretical stagnation point streamline (SPS). Interfaces are defined by the intersection of the SPS and material surfaces (white iso-contours). Reactants (light blue); Mixing (blue); Weakly reacting (orange); Strongly reacting (red); Products (green). The magenta arrow shows the x_s origin.

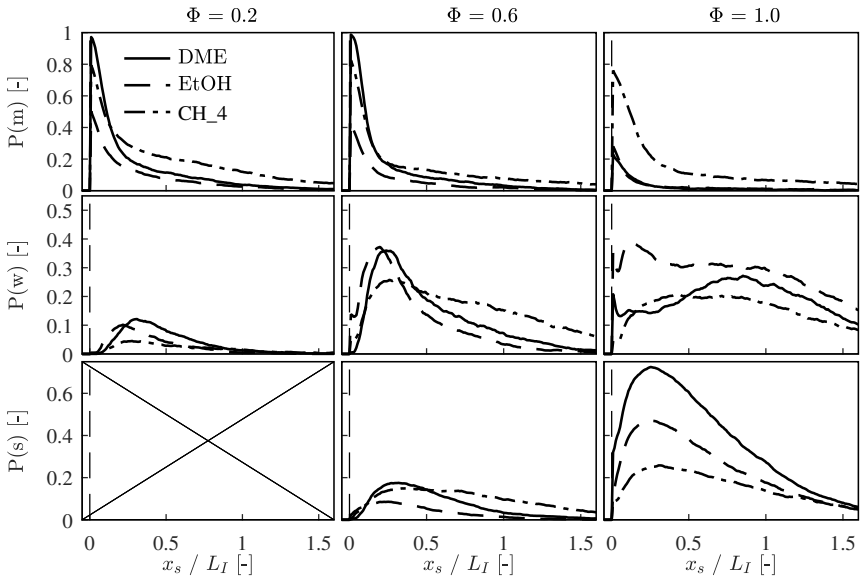

Fig. 4: Multi-fluid probability (P) statistics for DME, EtOH and CH_4 combustion with varying Φ along the stagnation point streamline with data aligned at the x_s = 0 iso-contour. Top row: Mixing fluid probability ($P(m)$); Middle row: Weakly reacting fluid probability ($P(w)$); Bottom row: Strongly reacting fluid probability ($P(s)$); First column: Φ = 0.20; Second column: Φ = 0.60; Third column: Φ = 1.0.

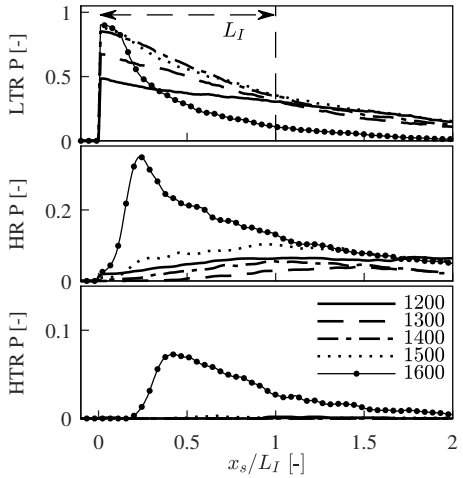

Fig. 5: Multi-fluid probability statistics along the SPS and aligned at x_s = 0. Low temperature reactive (top), heat release (middle) and high temperature reactive fluid (bottom). Legend: T_{HCP} in [K].

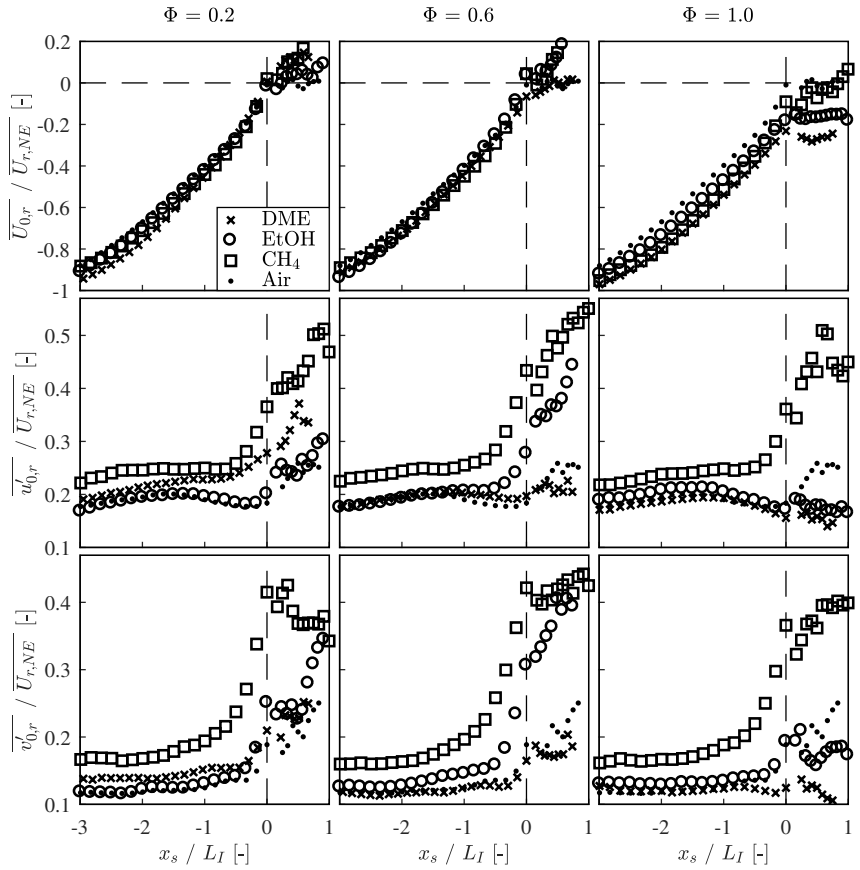

Fig. 6: Conditional mean axial reactant fluid velocity and the axial and radial fluctuation for DME, EtOH and CH_4 at varying Φ evaluated along the stagnation point streamline and aligned at x_s = 0. The dotted line indicates the mixing case (i.e. air with Φ = 0.0) for reference. Top row: $\overline{U_{0,r}}$ / $\overline{U_{r,NE}}$; Middle row: $\overline{u'_{0,r}}$ / $\overline{U_{r,NE}}$; Bottom row: $\overline{v'_{0,r}}$ / $\overline{U_{r,NE}}$; First column: Φ = 0.2; Second column: Φ = 0.6; Third column: Φ = 1.0.

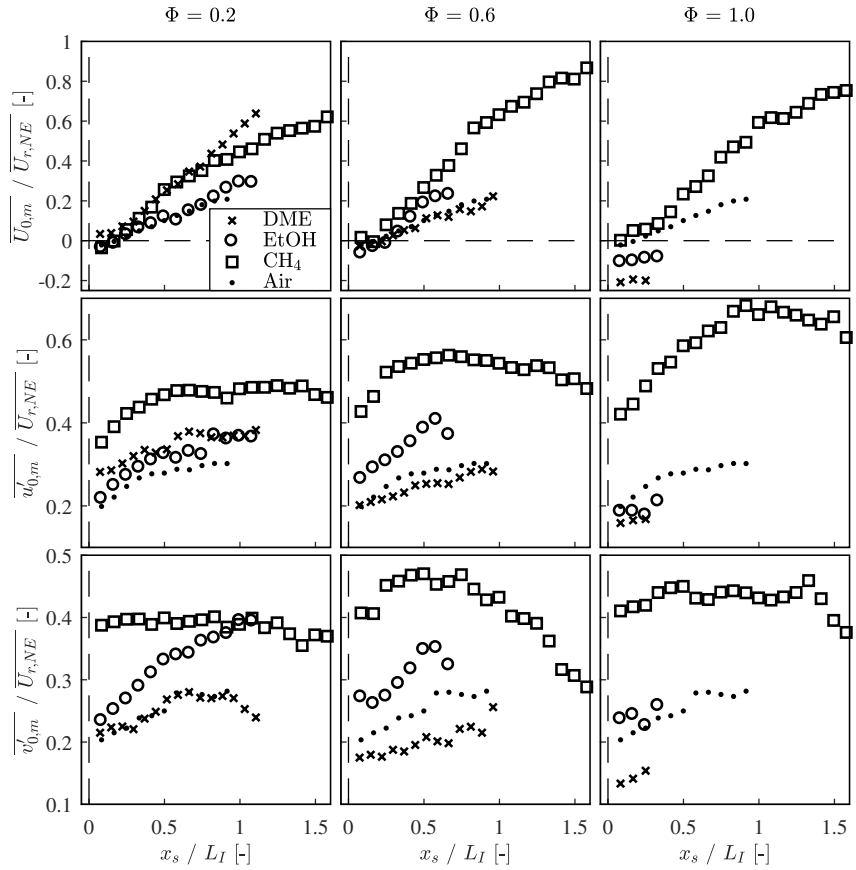

Fig. 7: Conditional mean axial mixing fluid velocity and the axial and radial fluctuations for DME, EtOH and CH_4 at varying Φ evaluated along the stagnation point streamline and aligned at x_s = 0. The dotted line indicates the mixing case (i.e. air with Φ = 0.0) for reference. Top row: $\overline{U_{0,m}}$ / $\overline{U_{r,NE}}$; Middle row: $\overline{u'_{0,m}}$ / $\overline{U_{r,NE}}$; Bottom row: $\overline{v'_{0,m}}$ / $\overline{U_{r,NE}}$; First column: Φ = 0.2; Second column: Φ = 0.6; Third column: Φ = 1.0.

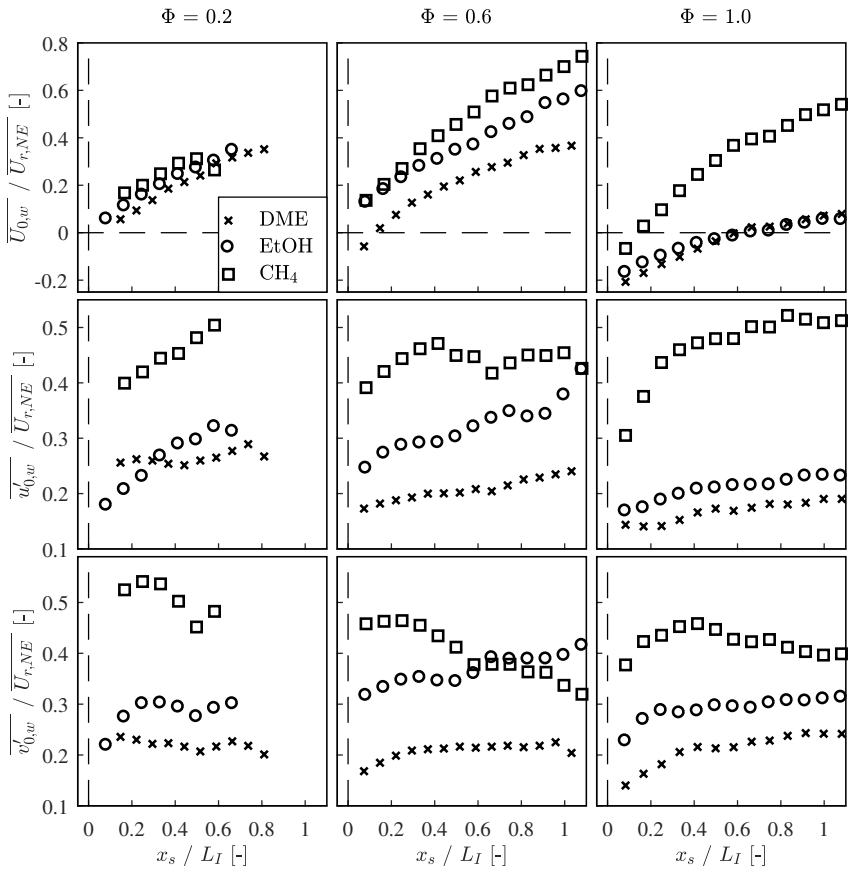

Fig. 8: Conditional mean axial weakly reacting fluid velocity and the axial and radial fluctuations for DME, EtOH and CH_4 at varying Φ evaluated along the stagnation point streamline and aligned at x_s = 0. Top row: $\overline{U_{0,w}}$ / $\overline{U_{r,NE}}$; Middle row: $\overline{u'_{0,w}}$ / $\overline{U_{r,NE}}$; Bottom row: $\overline{v'_{0,w}}$ / $\overline{U_{r,NE}}$; First column: Φ = 0.2; Second column: Φ = 0.6; Third column: Φ = 1.0.

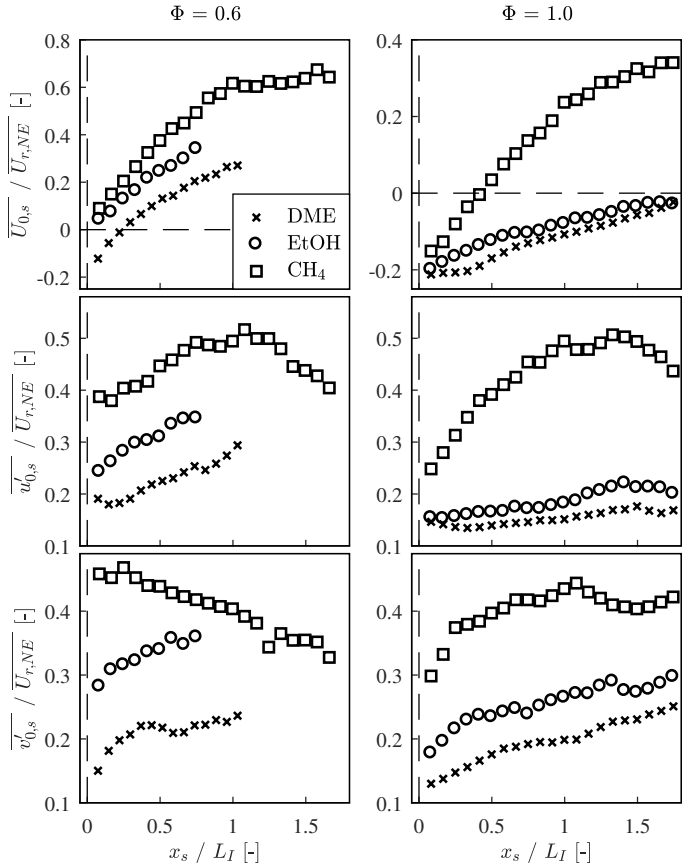

Fig. 9: Conditional mean axial strongly reacting fluid velocity and the axial and radial fluctuations for DME, EtOH and CH_4 at varying Φ evaluated along the stagnation point streamline and aligned at x_s = 0. Top row: $\overline{U_{0,s}}$ / $\overline{U_{r,NE}}$; Middle row: $\overline{u'_{0,s}}$ / $\overline{U_{r,NE}}$; Bottom row: $\overline{v'_{0,s}}$ / $\overline{U_{r,NE}}$; First column: Φ = 0.6; Second column: Φ = 1.0.

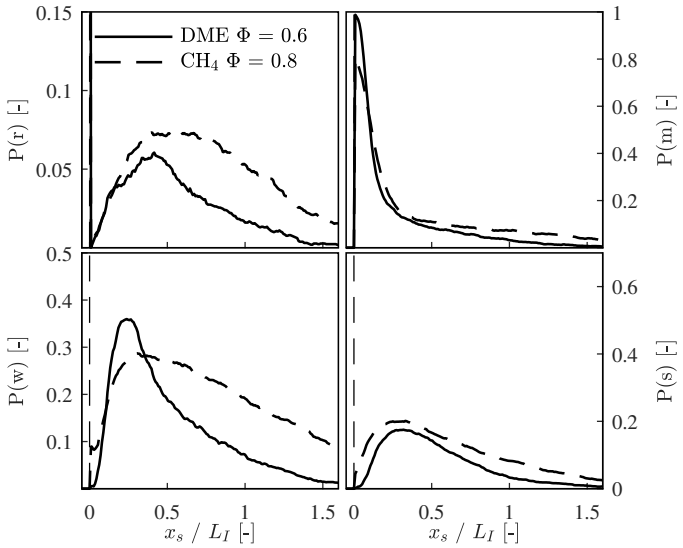

Fig. 10: Conditional multi-fluid probabilities for cases with similar Damköhler numbers (Da = 1.2 vs. 1.5; DME with Φ = 0.6 vs. CH_4 with Φ = 0.8). Top left: Reactant fluid probability $P(r)$; Top right: Mixing fluid probability $P(m)$; Bottom left: Weakly reacting fluid probability $P(w)$; Bottom right: Strongly reactant fluid probability $P(s)$.

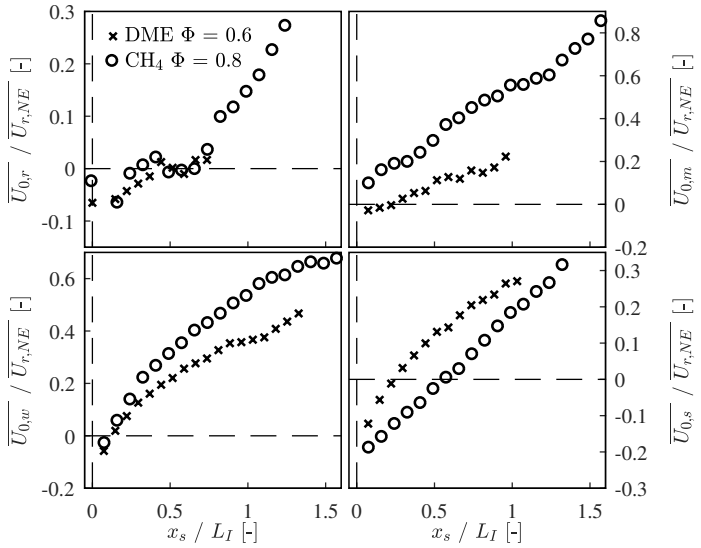

Fig. 11: Conditional mean axial fluid velocities for cases with similar Damköhler numbers (Da = 1.2 vs. 1.5; DME with Φ = 0.6 vs. CH_4 with Φ = 0.8). Top left: Reactant fluid velocity; Top right: Mixing fluid velocity; Bottom left: Weakly reacting fluid velocity; Bottom right: Strongly reactant fluid velocity.

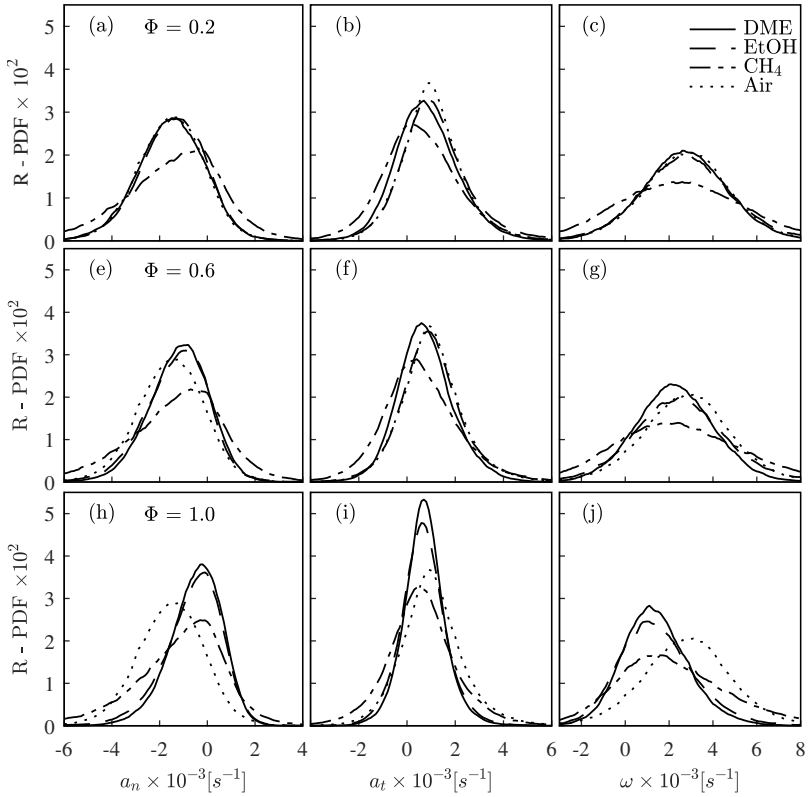

Fig. 12: PDF of the rate of strain along the reactant fluid surface (R) for DME, EtOH and CH_4 at varying Φ. The dotted line indicates the mixing case (i.e. air with Φ = 0.0) for reference. First column: Normal strain; Second column: Tangential strain; Third column: Vorticity. First row: Φ = 0.2; Second row: Φ = 0.6; Third row: Φ = 1.0.

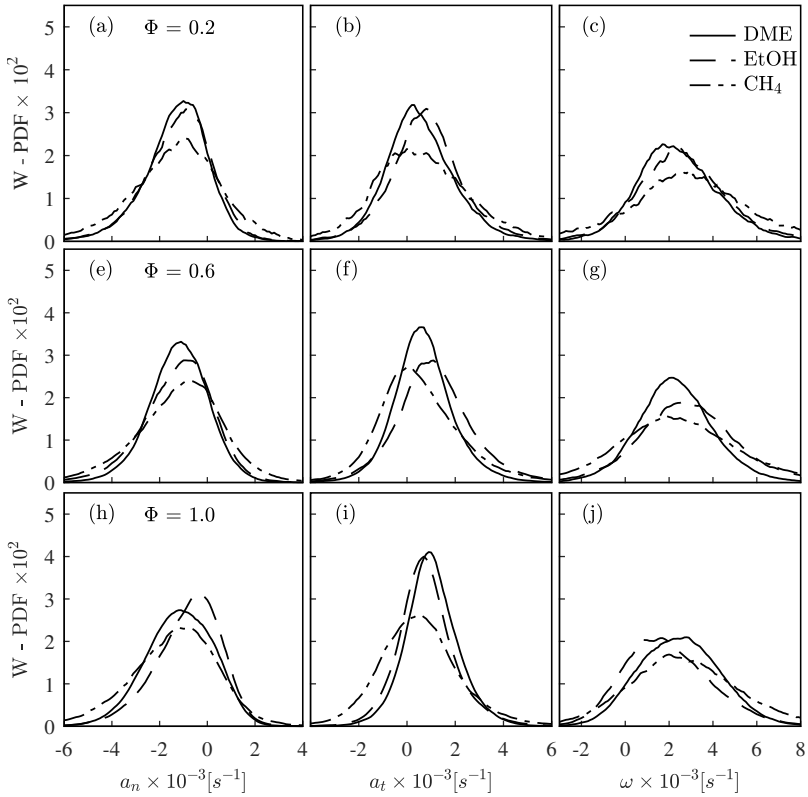

Fig. 13: PDF of the rate of strain along the weakly reacting fluid surface (W) for DME, EtOH and CH_4 at varying Φ: First column: Normal strain; Second column: Tangential strain; Third column: Vorticity. First row: Φ = 0.2; Second row: Φ = 0.6; Third row: Φ = 1.0.

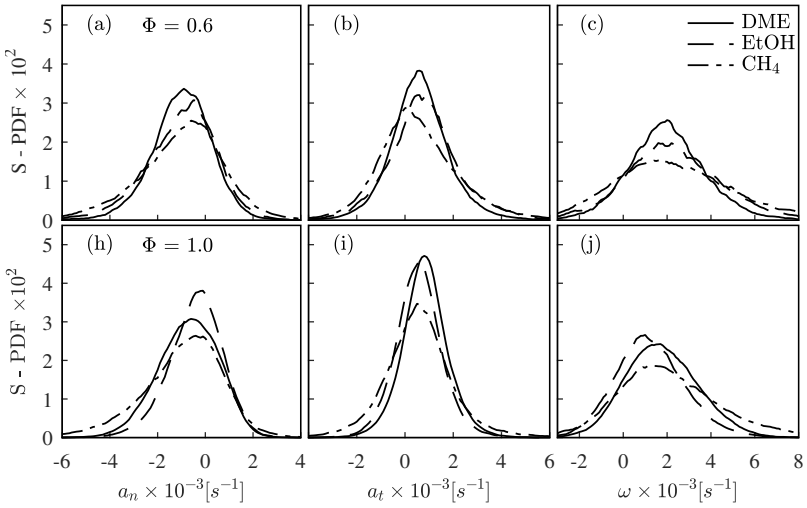

Fig. 14: PDF of the rate of strain along the strongly reacting fluid surface (S) for DME, EtOH and CH_4 at varying Φ: First column: Normal strain; Second column: Tangential strain; Third column: Vorticity. First row: Φ = 0.2; Second row: Φ = 0.6; Third row: Φ = 1.0.

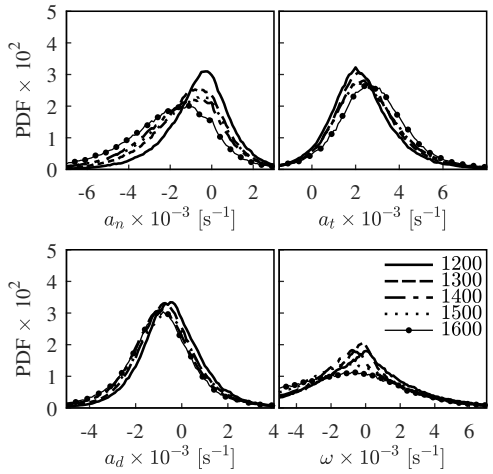

Fig. 15: Rate of strain and vorticity evaluated along the low temperature reacting fluid surface: Normal (top left), tangential (right) and total (bottom left) strain and vorticity (right). Legend: T_{HCP} in [K].

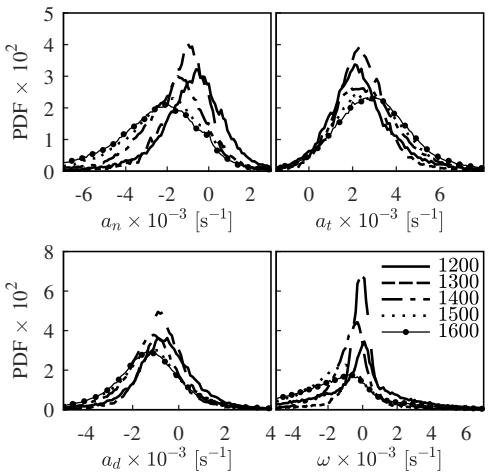

Fig. 16: Rate of strain and vorticity evaluated along the heat release material surface: Normal (top left), tangential (right) and total (bottom left) strain and vorticity (right). Legend: T_{HCP} in [K].